Materials **2011**, *4*, 651-702; doi:10.3390/ma4040651

OPEN ACCESS

materials

ISSN 1996-1944

www.mdpi.com/journal/materials

Review

Magnetoelectric Interactions in Lead-Based and Lead-Free Composites

Mirza Bichurin [1,*], Vladimir Petrov [1], Anatoly Zakharov [1], Denis Kovalenko [1], Su Chul Yang [2], Deepam Maurya [2], Vishwas Bedekar [2] and Shashank Priya [2]

[1] Institute of Electronic & Information System, Novgorod State University, 173003 Veliky Novgorod, Russia; E-Mails: vladimir.petrov@novsu.ru (V.P.); anatoly.zakharov@novsu.ru (A.Z.); denis.kovalenko@novsu.ru (D.K.)

[2] Center for Energy Harvesting Materials and Systems, Virginia Tech, Blacksburg, VA 24061, USA; E-Mails: ysc2573@gmail.com (S.C.Y.); mauryad@vt.edu (D.M.); vishwas@vt.edu (V.B.); spriya@vt.edu (S.P.)

* Author to whom correspondence should be addressed; E-Mail: mirza.bichurin@novsu.ru; Tel.: +7-8162-629-939; Fax: +7-8162-624-110.

Received: 10 February 2011; in revised form: 15 March 2011 / Accepted: 23 March 2011 / Published: 6 April 2011

Abstract: Magnetoelectric (ME) composites that simultaneously exhibit ferroelectricity and ferromagnetism have recently gained significant attention as evident by the increasing number of publications. These research activities are direct results of the fact that multiferroic magnetoelectrics offer significant technological promise for multiple devices. Appropriate choice of phases with co-firing capability, magnetostriction and piezoelectric coefficient, such as Ni-PZT and NZFO-PZT, has resulted in fabrication of prototype components that promise transition. In this manuscript, we report the properties of Ni-PZT and NZFO-PZT composites in terms of ME voltage coefficients as a function of frequency and magnetic DC bias. In order to overcome the problem of toxicity of lead, we have conducted experiments with Pb-free piezoelectric compositions. Results are presented on the magnetoelectric performance of Ni-NKN, Ni-NBTBT and NZFO-NKN, NZFO-NBTBT systems illustrating their importance as an environmentally friendly alternative.

Keywords: multiferroics; lead-free piezoelectrics; morphotropic phase boundary; magnetoelectric effect

---

1. Introduction

The realization of a material with simultaneous presence of strong electric and magnetic order at room temperature, termed 'multiferroics', would be a milestone for modern electronics and multifunctional materials. Multiferroic magnetoelectric (ME) materials become magnetized when placed in an electric field, and conversely electrically polarized when placed in a magnetic field. Dielectric polarization of a material under a magnetic field, or an induced magnetization under an electric field, requires the simultaneous presence of long-range ordering of magnetic moments and electric dipoles [1-4]. These materials offer potential for new generations of sensor, filter, and field-tunable microwave dielectric devices [5].

A suitable combination of two phases can yield the magnetoelectric property, such as combination of piezomagnetic and piezoelectric phases or combination of magnetostrictive and piezoelectric phases which will give rise to ME effect. ME effect can also realized by coupled thermal interaction in pyroelectric–pyromagnetic composites. The ME effect obtained in composites is more than one hundred times that of single–phase ME material such as Cr_2O_3. Suchtelen and Boomgaard outlined the conceptual points inherent to the ME effect in composites [6,7]. These can be summarized as: (i) Two individual phases should be in equilibrium (ii); Mismatching between grains should not be present (iii); Magnitude of the magnetostriction coefficient of piezomagnetic or magnetostrictive phase and magnitude of the piezoelectric coefficient of the piezoelectric phase must be greater (iv); The accumulated charge must not leak through the piezomagnetic or magnetostrictive phase; and (v) Deterministic strategy for poling of the composites. In spite of the promise of large magnetoelectric (ME) coefficients in elastically coupled nano-composites, experimental investigations for a number of configurations have not yielded values approaching those predicted by continuum mechanics and *ab-initio* calculations. The understanding of the physical interaction occurring in the composites with multi-dimensional connectivity between the magneto-elastic stresses and elastoelectric fields has not been achieved. The lack of this understanding has limited the ability to achieve the theoretical response of the material by coordinating the local electro-magnetic couplings, via coherent elastic interactions between phases. In these materials the theory predicts the size of the ME coefficient to be more than 5 V/cm.Oe. In order to understand the phenomenon of magnetoelectrics in composites comprised of individual piezoelectric and magnetostrictive phases, it will be important to develop theory and experiments that identify the effect of various physical and mechanical parameters on the magnitude of the magnetoelastic and elastoelectric coupling.

The discrepancy between theoretical and experimental values of ME voltage coefficients can also be attributed to the use of a one-dimensional approach. A series of studies by the authors have attempted to address these issues in their models. The suggested method consists of deriving the effective material parameters of composites and is carried out in two stages. In the first stage, the composite is considered as a structure consisting of piezoelectric and magnetostrictive phases. Further, we consider only (symmetric) extensional deformation in this model and ignore any (asymmetric) flexural deformations of the components that would lead to position dependent elastic constants and the need for perturbation procedures. For the polarized piezoelectric phase with the symmetry ∞m, the following equations can be written for the strain and electric displacement:

$$
\begin{aligned}
{}^{p}S_i &= {}^{p}s_{ij}\,{}^{p}T_j + {}^{p}d_{ki}\,{}^{p}E_k \\
{}^{p}D_k &= {}^{p}d_{ki}\,{}^{p}T_i + {}^{p}\varepsilon_{kn}\,{}^{p}E_n
\end{aligned}
\tag{1}
$$

where ${}^{p}S_i$ and ${}^{p}T_j$ are strain and stress tensor components of the piezoelectric phase, ${}^{p}E_k$ and ${}^{p}D_k$ are the vector components of the electric field and electric displacement, ${}^{p}s_{ij}$ and ${}^{p}d_{ki}$ are compliance and piezoelectric coefficients, and ${}^{p}\varepsilon_{kn}$ is the permittivity matrix. The magnetostrictive phase is assumed to have a cubic symmetry and is described by the equations:

$$
\begin{aligned}
{}^{m}S_i &= {}^{m}s_{ij}\,{}^{m}T_j + {}^{m}q_{ki}\,{}^{m}H_k \\
{}^{m}B_k &= {}^{m}q_{ki}\,{}^{m}T_i + {}^{m}\mu_{kn}\,{}^{m}H_n
\end{aligned}
\tag{2}
$$

where ${}^{m}S_i$ and ${}^{m}T_j$ are strain and stress tensor components of the magnetostrictive phase, ${}^{m}H_k$ and ${}^{m}B_k$ are the vector components of magnetic field and magnetic induction, ${}^{m}s_{ij}$ and ${}^{m}q_{ki}$ are compliance and piezomagnetic coefficients, and ${}^{m}\mu_{kn}$ is the permeability matrix. Equation (2) may be considered as a linearized equation describing the effect of magnetostriction. Using appropriate boundary conditions, the ME voltage coefficients can be obtained by solving Equations (1) and (2).

In the second stage, the composite is considered to be homogeneous and the behavior is described by:

$$
\begin{aligned}
S_i &= s_{ij}T_j + d_{ki}E_k + q_{ki}H_k \\
D_k &= d_{ki}T_i + \varepsilon_{kn}E_n + \alpha_{kn}H_n \\
B_k &= q_{ki}T_i + \alpha_{kn}E_n + \mu_{kn}H_n
\end{aligned}
\tag{3}
$$

where S_i and T_j are strain and stress tensor components, E_k, D_k, H_k, and B_k are the vector components of the electric field, electric displacement, magnetic field and magnetic induction, s_{ij}, d_{ki}, and q_{ki} are effective compliance, piezoelectric and piezomagnetic coefficients, and ε_{kn}, μ_{kn} and α_{kn} are effective permittivity, permeability and ME coefficient. Effective parameters of the composite are obtained by solving Equation (3) by taking into account solutions of Equations (1) and (2). The mechanical strain and stress for composite and homogeneous material are assumed to be the same and the electric and magnetic vectors are determined by using appropriate boundary conditions. This method has shown considerable success in modeling the response of ME composites.

As an example we illustrate the results obtained on L-T mode ME composites. This case corresponds to polarization field E_0 and AC electric field E perpendicular to the sample plane and bias field H_0 and AC magnetic field H parallel to the sample plane and the ME coefficient is given as $\alpha_{E,T} = \alpha_{E,31} = E_3/H_1$. In this case, non-zero components of ${}^{p}s_{ij}$, ${}^{p}d_{ki}$, ${}^{m}s_{ij}$, ${}^{m}q_{ki}$, s_{ij}, d_{ki}, q_{ki}, α_{kn} are determined by composite symmetry and Equations (1)–(3) are solved for appropriate boundary conditions. The expression obtained for transverse ME voltage coefficient is given below [8]:

$$
\alpha_{E,31} = \frac{E_3}{H_1} = \frac{-v(1-v)({}^{m}q_{11}+{}^{m}q_{21})\,{}^{p}d_{31}}{{}^{p}\varepsilon_{33}({}^{m}s_{12}+{}^{m}s_{11})v+{}^{p}\varepsilon_{33}({}^{p}s_{11}+{}^{p}s_{12})(1-v)-2\,{}^{p}d_{31}^{2}(1-v)}
\tag{4}
$$

where v is piezoelectric volume fraction. Equation (4) describes the dependence of ME parameters on volume fraction and is used to estimate the ME coupling for some representative systems. For a bilayer of nickel ferrite (NFO) and PZT the measured and calculated values of ME voltage coefficient equal about 240 mV/cm.Oe.

Investigations have revealed the presence of both ferroelectricity and magnetism in a number of materials such as perovskite type $BiFeO_3$, $BiMnO_3$, the boracite family, $BaMF_4$ compounds (M, divalent transition metal ions), hexagonal $RMnO_3$ (R, rare earths), and the rare earth molybdates, but none seem to provide large coupling between them [6-7,9-17]. Recently, rare earth manganites such as $TbMnO_3$, $DyMnO_3$, and $TbMn_2O_5$ have been reported to exhibit reproducible electric polarization under magnetic fields, however the magnitude of the magnetoelectric (ME) coefficient (unit of V/cm.Oe) is quite small [4,11,18-23]. Single phase materials suffer from the drawback that the ME effect is considerably weak even at low temperatures. Better alternatives to single phase materials are ME composites. The composites exploit the product property of the materials (the ME effect is not present in individual phases). Recently, the focus of much research has been on the laminated magnetoelectric composites made by using piezoelectric and magnetostrictive materials [24-43]. In our original work, we reported the results on laminate composites (MLCs) made from the giant magnetostrictive material, Terfenol-D, and relaxor-based piezocrystals $Pb(Mg_{1/3}Nb_{2/3})O_3$–$PbTiO_3$ (PMN-PT) [44]. Magnetoelectric behavior in laminate composites has now been reported for various material couples including $Pb(Zr,Ti)O_3$ (PZT) or $Pb(Mg_{1/3}Nb_{2/3}O_3$-$PbTiO_3$ (PMN-PT) layers laminated with magnetostrictive $Tb_{1-x}Dy_xFe_{2-y}$, Permendur, $Ni_{1-x}Co_xFe_2O_4$ (*i.e.*, NFO), or $Co_{1-x}Zn_xFe_2O_4$ (*i.e.*, CFO) ones [45-60]. Recently, Bichurin *et al*. found a giant enhancement in the magnitude of the bulk composites at the resonance frequency of the samples [61]. A high ME coefficient of 23000 mV/cm.Oe was reported for the samples with 80% PZT-20% Ni Ferrite (~350 kHz, sample diameter 10 mm), an increase by a factor of 600 as compared to the data at low frequency (~1 kHz).

Figure 1 shows some examples of the structures that can be designed using the two phases in thin film and bulk forms. It can be seen from this figure that the possibilities are numerous and there can be several phases (amorphous, ceramic, metal, polymer, *etc*.), shapes (disk, cylinder, plate, toroid, sphere, *etc*.), and sizes (number of layers, layer thicknesses, length and width can be varied differently) for obtaining the magnetoelectric properties. It is important to note here that all of these combinations will exhibit ME response with varying degree of magnitude. For n phases the number of connectivity patterns is given as $(n+3)!/3!n!$, which for two phase composites comes out to be 10, for three phases as 20, and 35 for four phase pattern. Further, in each of these shapes there is the possibility of orienting the polarization along different axes and applying the electric (E) and magnetic (H) fields along different axes. In addition there are several choices for materials depending on magnetostriction constant, resistivity, permeability, permittivity, piezoelectric strain and voltage constant, sintering temperature, and chemical reactivity (Magnetostrictive-$MnFe_2O_4$, $CoFe_2O_4$, $NiFe_2O_4$, $ZnFe_2O_4$, YFe_5O_{12}, $SmFe_5O_{12}$, YIG, Terfenol-D, Metglas 2605SC, Ni, Co, *etc*.; Piezoelectric-PZT, $BaTiO_3$, PMN-PT, PVDF, $SrBi_4Ti_4O_{15}$, $(Na_{0.5}K_{0.5})NbO_3$) *etc*.).

Figure 1. Schematics of the magnetoelectric composites illustrating the multiple possibilities **(a)** self-assembled nano-pillar structures; **(b)** layer by layer deposition; **(c)** deposition accompanied by masking and patterning; **(d)** three phase deposition for gradient materials; **(e)** particles dispersed in a polymer matrix; **(f)** lamination; **(g)** checkerboard arrangement; **(h)** sintered particulates; and **(i)** variation in poling, applied field direction and measuring electrodes.

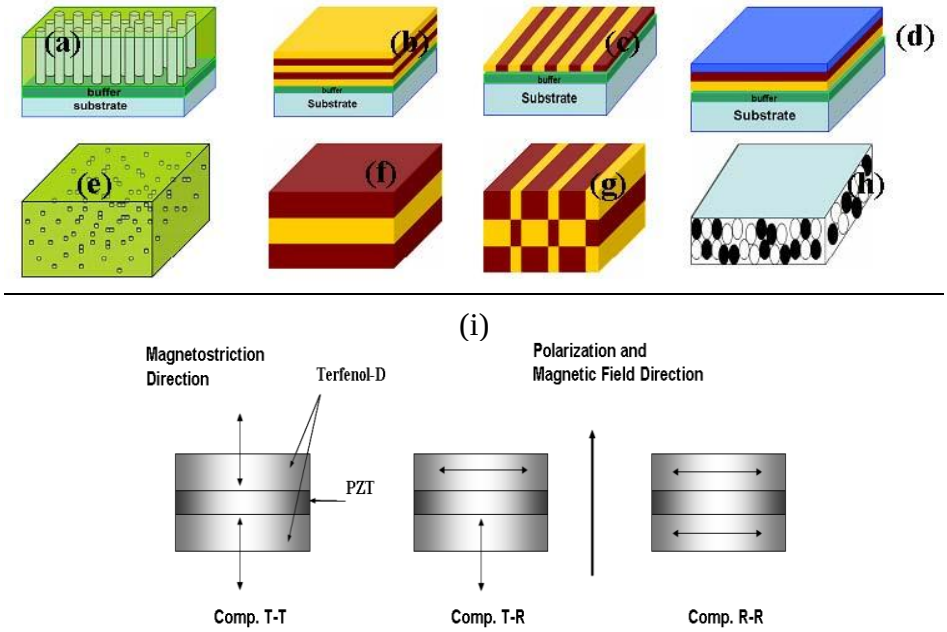

$Pb(Zr,Ti)O_3$ (PZT) based ceramics have excellent dielectric and piezoelectric properties and are currently the dominant material system for actuators, sensors and resonators. However, the Pb element in these materials presents an environmental problem. Thus, the research is now focused on finding an alternative for PZT's. In the past two decades, several publications and patents have reported on lead-free piezoelectrics. Out of all the possible choices, $(Na,K)NbO_3$ (NKN) based ceramics (e.g., solid solution of NKN-$LiNbO_3$ [62], NKN-$LiTaO_3$ [63], NKN-$LiSbO_3$ [64], NKN-$Li(Nb, Ta, Sb)O_3$ [65], NKN-$BaTiO_3$ [66], NKN-$SrTiO_3$ [67,68], and NKN-$CaTiO_3$ [69]) have received considerable attention mainly for two reasons: (i) piezoelectric properties exist over a wide range of temperature, and (ii) there are several possibilities for substitution and additions. An interesting possibility arises from the fact that if one can find a high piezoelectric performance lead–free ceramics and combine it with magnetostrictive material with high piezo-magnetic coefficient to achieve environment friendly magnetoelectric materials with desired sensitivity.

We have conducted extensive studies on phase transitions, synthesis, and piezoelectric/dielectric properties of $(1 - x)(Na_{0.5}K_{0.5})NbO_3$-$xBaTiO_3$ ceramics ($0.0 \leq x \leq 1.0$). This system exhibits three phase transition regions corresponding to orthorhombic, tetragonal, and cubic phases. The composition $0.95(Na_{0.5}K_{0.5})NbO_3$-$0.05BaTiO_3$, which lies on boundary of orthorhombic and tetragonal phase, was found to exhibit excellent piezoelectric properties. The properties of this composition were further improved by addition of various additives making it suitable for multi-layer actuator application. The composition $0.06(Na_{0.5}K_{0.5})NbO_3$-$0.94BaTiO_3$ was found to lie on the boundary of tetragonal and cubic phase. This composition exhibited the microstructure with small grain size and excellent

dielectric properties suitable for multi-layer ceramic capacitor application. In the next section, we summarize the progress made in the field of lead-free piezoelectric materials.

2. Progress on Lead–Free Piezoelectric Materials

Most of the investigated lead-free piezoelectric systems are based on $Na_{0.5}Bi_{0.5}TiO_3$ (NBT) and $K_{0.5}Na_{0.5}NbO_3$ (NKN) compositions. This section briefly describes the progress made on these two lead-free piezoelectric materials.

2.1. NBT-BT Lead-Free Piezoelectric

$Na_{0.5}Bi_{0.5}TiO_3$ (NBT) was discovered by Smolenskii [70] in 1961. It was reported that NBT is a relaxor ferroelectric with diffuse phase transition from rhombohedral to tetragonal phase between 200 ℃ and 320 ℃ and from tetragonal to cubic phase at 540 ℃ [71-74]. The region between 200–320 ℃ has been subject of intense discussions related to the existence of antiferroelectric phase. Some researchers have suggested coexistence of rhombohedral and tetragonal phases in this temperature range with polar nano regions [75]. However in a recent work, *in situ* temperature dependent TEM studies showed phase transition from ferroelectric rhombohedral to anti-ferroelectric orthorhombic phase proceeded via an antiferroelectric modulated phase consisting of orthorhombic sheets in a rhombohedral matrix in the temperature range from 200–300 ℃. A second phase transition from O-T phase occurs near 320 ℃, which corresponds to the antiferroelectric/paraelectric phase transition.

The solid solution of NBT with various tetragonal compounds has been investigated including $K_{1/2}Bi_{1/2}TiO_3$ (KBT), $BaTiO_3$, $CaTiO_3$, $SrTiO_3$ and $PbTiO_3$ [76-79]. Takenaka *et al*. [79] presented the phase diagram of NBT-BT showing the existence of a morphotropic phase boundary (MPB). The longitudinal piezoelectric constant (d_{33}) for NBT-6% BT composition was found to be 125 pC/N along with k_{33} of 55% and loss tangent factor of 1.3%. However, Curie temperature (T_c) and ferroelectric to anti-ferroelectric transition temperature (T_d, also referred as depoling temperature) decreased at MPB. In comparison to lead-based perovskites, NBT has higher elastic modulus (~110 GPa *vs*. 70 GPa) and lower density (6 g/cm^3) which makes it favorable for light-weight actuation applications [76]. Modification with $BiScO_3$ and $BiFeO_3$ lead to increment in T_c of NBT and NBT-BT up to 400 ℃ together with an improvement of remnant polarization (P_r) [80-82]. Li *et al*. [83] have reported the dielectric and piezoelectric response of $(1 - x)(Na_{0.5}Bi_{0.5})TiO_3$-$xNaNbO_3$ ceramics. The samples in composition range of 0.01 to 0.02 were found to exhibit d_{33} ~80–88 pC/N. In recent work, effect of Na non-stochiometry in $Bi_{0.5}Na_{0.5-x}TiO_3$ ceramics was investigated [84] The grain size was found to decrease with increase in Na non-stoichiometry. However, d_{33} was increased from 74 pC/N (T_d ~190 ℃) at x = 0.0 to 91 pC/N (T_d ~112 ℃) at x = 3.5 and then dropped with further Na deficiency. The effect of bismuth excess on NBT-BT ceramics near MPB and compositions with $x \leq 0.505$ was positive leading to large P_r ~37.5 − 41.1 μC/cm^2 and d_{33} ~171–176 pC/N at RT with moderate depoling temperature (T_d) ~85 ℃ [85]. Wang *et al*. [86] have studied $(0.95 - x)(Bi_{1/2}Na_{1/2})TiO_3$-$x(Bi_{1/2}K_{1/2})TiO_3$-$0.05BaTiO_3$; x = 0–20 mol% compositions and specimen with x = 5 mol% were found to exhibit d_{33} ~148 pC/N, k_p~34 %, k_t~49.2 % and T_d ~125 ℃. However, these modifiers also increased the magnitude of coercive field (E_c) which makes the poling difficult. Generally, E_c and T_d are lower in doped materials, however cobalt doping was found to enhance T_d by 20 ℃ [87,88]. High piezoelectric

properties in these Bi based compounds is always accompanied with the lowering of T_d as shown in Figure 2. Lower T_d leads to unstable domains which are easy to switch and hence give rise to higher piezoelectric constant [87]. Li doping of 4 at% in NBT-BT has been found to improve the piezoelectric coefficient as d_{33} = 176 pC/N, k_{33} = 0.6 and T_d = 171 ℃ [89]. In order to further improve the piezoelectric response without lowering the depoling temperature (T_d) various researchers have used reactive template (RTGG) and template (TGG) grain growth method [90-95] to texture the ceramics. The $<100>_c$ textured 0.94NBT-0.06$BaTiO_3$ ceramics was found to exhibit d_{33} ~241 pC/N, k_p ~41.2 % and k_t ~66.5% at RT with T_d ~115 ℃.

Investigations on growth of lead-free single crystals in NBT-BT systems has shown that near MPB compositions are congruently melting and can be grown by flux growth [96] and top seeded solution growth (TSSG) method [97]. Recently, longitudinal piezoelectric constant (d_{33}) as high as 457 pC/N with k_{33} ~68.5 % was reported on Mn doped NBT-BT single crystal grown by TSSG method. Piezoelectric properties of various NBT-based materials are listed in Table 1 along with other prominent lead-free piezoelectric materials. In order to demonstrate practical feasibility, Chen *et al*. [98] investigated high frequency ultrasonic transducers with NBT-BT lead-free single crystal as the active element. The (001) oriented NBTBT crystal was found to exhibit a thickness mode electromechanical coupling coefficient k_t of ~0.52 and low clamped dielectric constant of ~80.

Figure 2. Variation of the piezoelectric constant and transition temperature (ferroelectric to antiferroelectric phase mentioned as depolarization temperature) as a function of $BaTiO_3$ concentration in NBT–BT system.

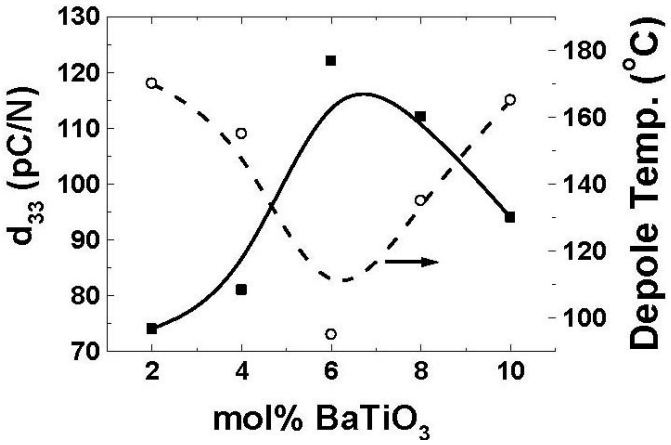

Recently, giant electric field induced strain (~0.45%) was observed in (1 − x − y) $(Bi_{0.5}Na_{0.5})TiO_3$-x$BaTiO_3$-y$(K_{0.5}Na_{0.5})NbO_3$ceramics [99-101]. The MPB composition 0.94$(Bi_{0.5}Na_{0.5})TiO_3$-0.06$(BaTiO_3)$ exhibited field induced ferroelectricity and remained ferroelectric after field removal [102]. On addition of KNN, these ceramics were found to exhibit giant strain due to the full recovery of original dimensions for every electric cycle [103]. It turned out that addition of KNN lowered the transition temperature (T_d) [104]. Moreover, large electric field-induced strain in BNT-BT-KNN was attributed to a field induced transition from the antiferroelectric to the ferroelectric phase and explained in terms of change in the unit cell volume.

2.2. NKN Based Lead-Free Piezoelectric

Potassium sodium niobate ($Na_xK_{(1-x)}NbO_3$), is considered a promising lead-free piezoelectric material with high Curie temperature exhibiting ferroelectric properties over a wide temperature range. It is well known that the composition corresponding to 0.5/0.5 in the $NaNbO_3$–$KNbO_3$ system, abbreviated as NKN, has the maximum in the piezoelectric properties. NKN undergoes a structural phase transformation sequence on cooling of paraelectric Cubic (C) $\xrightarrow{\sim 415^{o}C}$ ferroelectric Tetragonal (T) $\xrightarrow{\sim 210^{o}C}$ ferroelectric Orthorhombic (O) $\xrightarrow{\sim -150^{o}C}$ ferroelectric Rhombohedral (R). The T→O boundary is known as the polymorphic phase boundary (PPB) to designate its difference with the MPB. The PPB of KNN solutions is nearly independent of x, remaining unchanged in temperature for $0 < x < 1$. This is in distinct contrast to the MPB for PZT, which is nearly independent of temperature, and fixed near $x = 0.5$. Figure 3 (a) and (b) shows the radial mode electromechanical coupling factor (k_p) and mechanical quality factor (Q_m) as a function of temperature for NKN. It can be clearly seen from this figure that piezoelectric properties remain almost constant until the FE_t phase appears at 180 ℃. The magnitude of k_p at room temperature is of the order of 0.456 and Q_m is around 234. Since in this system the high temperature phase (FE_t) is also ferroelectric there is no danger of depoling on exceeding the transition temperature. This provides a considerable advantage over the competing NBT-KBT and NBT-BT systems and for this reason KNN ceramics are the most promising high piezoelectric nonlead system.

Figure 3. Temperature dependence of piezoelectric properties for KNN. **(a)** Radial mode coupling factor and **(b)** Mechanical quality factor.

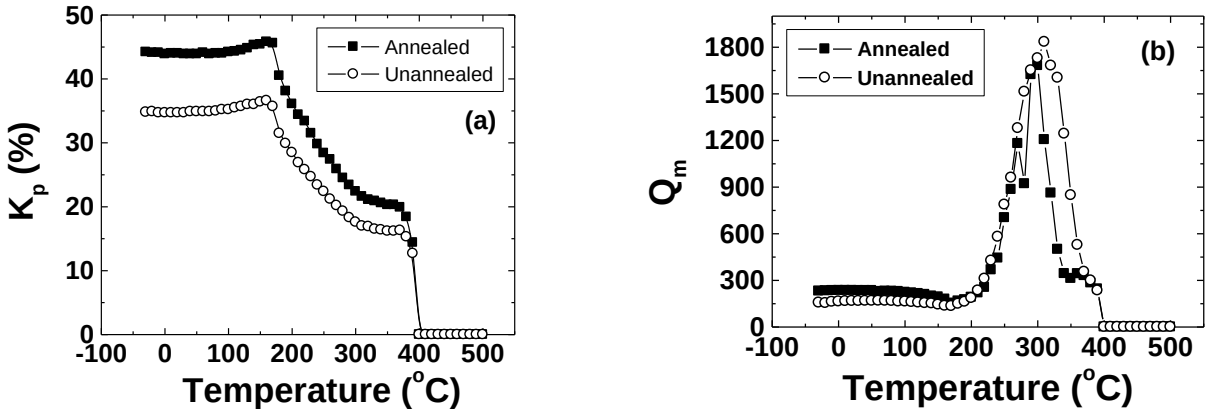

NKN ceramics are difficult to sinter and exhibit poor aging characteristics in air. The volatile nature of constituent materials gives rise to phase instability at high temperature, as above 1100 ℃ alkali deficiency may result in formation of secondary phase exhibiting abnormal grain growth [105]. Hot pressed specimens have been found to show dense microstructure with theoretical density higher than 99% leading to higher coupling constant (~0.48) and d_{33} value (~160 pC/N) as compared to ceramics processed through conventional sintering [106-108]. Spark plasma sintering [109,110] has also been shown to provide high relative density of 98%, however d_{33} value was nominal with a magnitude in the vicinity of 158 pC/N.

Piezoelectric properties of NKN based ceramics are a function of orthorhombic (O) to tetragonal (T) phase transition [111]. Ahn *et al.* [111] performed Rietveld and powder diffraction analysis to establish correlation between piezoelectric response, fraction of O and T phases, and NKN ratio for three different systems of (K,Na)NbO_3-$BaTiO_3$ (NKN-BT) NKN-$LiNbO_3$ (LN), and (K,Na,Li)NbO_3 (KNLN)-BT. It was found that higher piezoelectric properties in NKN based ceramics correlates with higher fraction of T phase and NKN ratio, where maximum piezoelectric properties are found in T-rich phase region with fraction of 70% and NKN ratio of 0.95. Several researchers [112,113] have studied the effect of the Na/K ratio in NKN system in order to improve the piezoelectric properties. Guo *et al*. [62] have studied the effect of Li-doping on piezoelectric properties of NKN by synthesizing the samples $Li_x(Na_{0.5}K_{0.5})(1 - x)NbO_3$(NKLN), for x varying between 0.0 to 0.2. A sharp peak in piezoelectric properties (d_{33} ~235 pC/N, k_p ~44 %) was observed in the composition range of $0.05 < x < 0.07$. Temperature dependent dielectric response of optimum composition revealed shifting of T_c and $T_{o\text{-}t}$ in opposite directions. Zhao *et al*. [114] reported that Li-modified NKN ceramics exhibit orthorhombic to tetragonal phase transition, which is similar to morphotropic phase boundary (MPB) and hence exhibit high piezoelectric constant (d_{33}~314 pC/N). Zhang *et al*. [115] substituted 0.058 mole % of Li^+ on A-site while B-site was substituted with Sb^{5+} in range of 2–8 mol % resulting in drastic shifting of T_{o-t} to 60 ℃. However, piezo-response was improved to d_{33} ~298 pC/N with k_p ~34.5%. Zhang *et al*. [64] in an extension of this work, synthesized the composition $(Na_{0.5}K_{0.5}Nb)_{(1-x)}(LiSb)_xO_3$ with x = 0.048–0.056. The composition with x = 0.052 was found to exhibit optimum piezoelectric properties (d_{33} ~286, and k_p ~0.51). This improvement in electromechanical properties was attributed to lowering of T_{o-t} transition temperature. Some of the significant NKN based piezoelectric materials has been summarized in Table 1.

Table 1. Dielectric and piezoelectric properties of the prominent lead-free systems.

Materials	**d_{33}**	**k_p**	**k_{33}**	**T_c**	**T_{o-t}/T_d**	**Reference**
$BaTiO_3$	190	0.36	0.5	115	0	[116]
BT-BCN	330	0.43		80	--	[117]
NBT-KBT-LBT	216	0.401		350	160	[118]
NBT-KBT-BT	183	0.367	0.619	290	100	[119]
NBT-xBT; x = 6–8%	122–176	0.21–0.36		225–228	90–105	[87,120–124]
NBT-6BT+7.5L	208	0.368		260	85	[125,126]
NBT-6BT-2NKN	30			260		[100,101]
NBT-20KBT (MPB)	140–190	0.27–0.35		280–300	130–170	[127-132]
$(K_{0.5}Na_{0.5})NbO_3$ (H.P.)	127	0.46	0.6	420		[107,108]
$(K_{0.5}Na_{0.5})NbO_3$	80	0.35	0.51	420	195	[133]
NKN-Li (7%)	240	0.45	0.64	460	~20	[134]
NKN-LF4(Textured)	410	0.61	-	253	25	[91,135]
NKN-SrTiO3 (5%)	200	0.37	-	277	27	[67,68]
NKN-LiTaO3 (5%)	200	0.36	-	430	55	[63]
NKN-LiNbO3 (6%)	235	0.42	-	460	70	[62]
NKN-$LiSbO_3$ (5%)	283	0.50	-	392	45	[64]

In past years, we have extensively analyzed the sintering and grain growth processes in PPB systems. The microstructures of the compositions close to PPB were investigated in order to clarify the sintering behavior of the KNN based lead-free ceramics. Figure 4 illustrates the schematic diagram of our sintering model. The changes in the microstructure are shown as a function of temperature. Figure 5 shows the SEM images of the specimens sintered at various temperatures for the composition $0.995(K_{0.48}Na_{0.48}Li_{0.04})NbO_3$-$0.005BaTiO_3$ (KLNN-BT). It has been shown before that KNN based ceramics exhibit cuboidal grains in the sintered microstructure. However, we found that the PPB composition ceramics rather consist of stacked structure of plate-like grains as schematically depicted in Figure 4 and experimentally observed in Figure 5. The rapid grain growth seen in this system was quantified by tracing the formation of liquid phase. These liquid phases are related to the formation of $K_3Li_2Nb_5O_{15}$ phase and Na-deficient KNLN-BT based phase formed by Na_2O evaporation. The liquid phase redistributes between the plates under the influence of capillary stress gradients. The grain growth could be modeled by Ostwald ripening.

Figure 4. Schematic diagrams of sintering model as a function of temperature in KNLN-BT based ceramics.

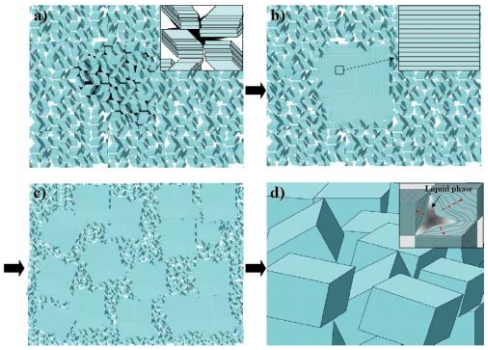

Figure 5. SEM images of the specimens sintered at various temperatures in KNLN-BT ceramics: **(a)** 950 ℃; **(b)** 980 ℃; **(c)** 1030 ℃; and **(d)** 1080 ℃.

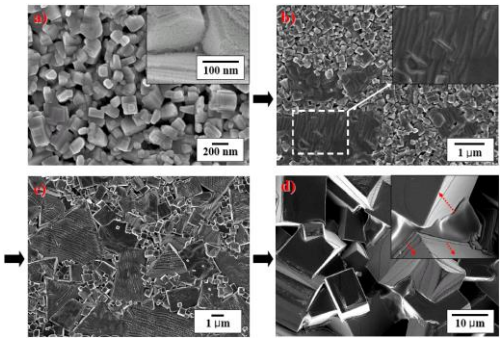

Recently in ABO_3 type perovskite, an interesting trend between atomic weight ratio of A and B sites ($R_w = W_A/W_B$) and piezoelectric constant (d_{33}) was demonstrated irrespective of tolerance factor (F_t) [136]. Most of the piezoelectric compositions were shown to exhibit large response when R_W for *A*-site heavy perovskites and $1/R_W$ for *B*-site heavy perovskites was higher than 2.0. Using this rule, KNN-based $[0.99(K_{0.48}Na_{0.48}Li_{0.04})(Nb_{1-x}Sb_x)O_3 - 0.01BaTiO_3]$ composition with d_{33} of 294 pC/N was designed.

Various researchers have grown KNN based single crystals. Pure KNN single crystals exhibited d_{33} ~160 pC/N [137] and Mn doped KNN single crystals were reported to possess d_{33} ~270 pC/N, T_{o-t} ~193 ℃ and *T*c ~416 ℃ [137,138]. Recently, $K_{0.5}Na_{0.5}NbO_3$-$LiNbO_3$ (KKN-LN) single crystals were grown using Bridgeman technique by Xu *et al*. [139]. These KNN-LN single crystals exhibit d_{33} ~405 pC/N and k_t ~61% with T_c ~428 ℃. However, composition fluctuation in single crystal is a critical issue and also their growth process is not cost-effective. Therefore, texturing of ceramics is gaining prominence as a potential alternative to single crystal. Saito *et al*. [91] reported that Li^+, Ta^{5+} and Sb^{5+} substituted <001> oriented KNN exhibits d_{33} ~416 pC/N, but these substitutions shifts PPT from 200 ℃ to near room temperature (RT) giving rise to temperature dependent behavior. Recently, Chang *et al*. [140] reported that textured $(K_{0.5}Na_{0.5})(Nb_{0.97}Sb_{0.3})O_3$ piezoelectric ceramics exhibits d_{33} ~208–218 pC/N, k_p ~0.64%, T_{o-t} ~160 ℃ and T_c ~352 ℃, which was superior than random KNN based ceramics of same composition.

3. Modeling of Piezoelectric Materials

3.1. Single Domain Approximation in Computing the Piezoelectric Coefficients of Ferroelectrics

To explain the physical properties and ferroelectric transitions, the Landau-Ginsburg-Devonshire (LGD) phenomenological approach was successfully used. The free energy expansion coefficients are usually determined from experimental data on permittivity and spontaneous polarization. For this purpose, the first principle calculations are used. However, a more complete expansion of free energy density is necessary to estimate the physical parameters of some single crystals in a wide temperature range.

The main objective of this work is to investigate the influence of ferroelectric composition on dielectric and piezoelectric parameters. We consider $PbTiO_3$, $BaTiO_3$, $LiTaO_3$, $KNbO_3$, $(Na_{0.5}K_{0.5})NbO_3$, and $Na_{0.5}Bi_{0.5}TiO_3$-$BaTiO_3$. We use the most appropriate expansions of free energy density to calculate the needed parameters.

3.1.1. Lead Titanate

Free energy density of a ferroelectric is defined by the expression:

$$F = F_f + F_e + F_{es} + F_E, \tag{5}$$

where F_f is the ferroelectric ordering energy, F_e is elastic energy, F_{es} is electrostriction energy, and F_E is the ferroelectric's energy in an external electric field. The equilibrium polarization is assumed to be directed along the Z-axis. Using sixth order expansion for polarization components, the ferroelectric ordering energy takes the form:

$$F_f = a_1P_3^2 + a_{11}P_3^4 + a_{111}P_3^6 \tag{6}$$

where P is polarization, a_1, . , a_{111} are the dielectric stiffness coefficients. Elastic energy is defined as:

$$F_e = \frac{c_{11}}{2}(S_1^2 + S_2^2 + S_3^2) + c_{12}(S_1S_2 + S_1S_3 + S_2S_3) \tag{7}$$

where S_i is the strain tensor component, c_{11} and c_{12} are the stiffness coefficients. Electrostriction energy can be written as follows:

$$F_{es} = -q_{11}S_3P_3^2 - q_{12}(S_1 + S_2)P_3^2, \tag{8}$$

where q_{11} и q_{12} are the electrostriction coefficient. Ferroelectric's energy in an applied electric field has the following form:

$$F_E = -P_3 E_3 \tag{9}$$

where E is the external electric field. Strain tensor components can be calculated by using the boundary conditions for mechanically free sample as:

$$\begin{cases} \dfrac{\partial F}{\partial S_1} = 0, \\ \dfrac{\partial F}{\partial S_3} = 0, \\ \dfrac{\partial F}{\partial S_3} = 0 \end{cases} \tag{10}$$

Solving the set of equations (10) for strain components yields:

$$\begin{cases} S_1 = \dfrac{P_3^2(-c_{12}q_{11} + c_{11}q_{12})}{-2c_{12}^{\ 2} + c_{11}c_{12} + c_{11}^{\ 2}}, \\ S_2 = \dfrac{P_3^2(-c_{12}q_{11} + c_{11}q_{12})}{-2c_{12}^{\ 2} + c_{11}c_{12} + c_{11}^{\ 2}}, \\ S_3 = \dfrac{(q_{11}c_{11} - 2c_{12}q_{12} + c_{12}q_{11})P_3^2}{-2c_{12}^{\ 2} + c_{11}c_{12} + c_{11}^{\ 2}}. \end{cases} \tag{11}$$

Substituting the found expressions (11) into Equation (5) results in the following equation:

$$F = a_1P_3^2 + b\,P_3^4 + a_{111}P_3^6 - E_3P_3, \tag{12}$$

where

$$b = \frac{2a_{11}c_{11}^{\ 2} + 2c_{11}a_{11}c_{12} - c_{11}q_{11}^{\ 2} - 2c_{11}q_{12}^{\ 2} + 4q_{12}c_{12}q_{11} - q_{11}^{\ 2}c_{12} - 4a_{11}c_{12}^{\ 2}}{2(c_{11} + 2c_{12})(c_{11} - c_{12})}.$$

It follows from Equation (12) that taking into account the boundary conditions for mechanically free sample results in re-normalization of ferroelectric stiffness coefficient for fourth order of polarization in the ferroelectric energy density. To find the equilibrium polarization of the sample, one should use the following equation:

$$\frac{\partial F}{\partial P_3} = -E_3. \tag{13}$$

where F is defined by Equation (12). The solution of Equation (13) has the form:

$$P_3 = \frac{\sqrt{-\dfrac{3b - 3\sqrt{b^2 - 3a_{111}a_1}}{a_{111}}}}{3} \tag{14}$$

Thus, the solution of Equations (10) and (13) enables finding of the equilibrium polarization and strain components that appear in Equation (5). Piezoelectric coefficients can be determined by using the equations for strains:

$$d_{ik} = \frac{\partial S_i}{\partial P_k} \chi_{kk}, \tag{15}$$

where $\chi_{kk} = \left(\frac{\partial^2 F}{\partial P_k^2} \right)^{-1}$ is dielectric susceptibility and, S_i are determined by Equation (11). Using Equations (15) and (11) we can find:

$$d_{33} = \frac{2P_3(2q_{12}c_{12} - c_{11}q_{11} - c_{12}q_{11})}{(2c_{12}^2 - c_{11}^2 - c_{11}c_{12})(2a_1 + 12bP_3^2 + 30a_{111}P_3^4)}, \tag{16}$$

$$d_{31} = \frac{2P_3(c_{11}q_{12} - c_{12}q_{11})}{(2c_{12}^2 - c_{11}^2 - c_{11}c_{12})(2a_1 + 12bP_3^2 + 30a_{111}P_3^4)}, \tag{17}$$

The permittivity can be found from the following equation:

$$\varepsilon_{33} = \left(\frac{\partial^2 F}{\partial P_3^2} \right)^{-1} + \varepsilon_0 \tag{18}$$

As an example, the parameters of lead titanate are estimated at room temperature T = 25 °C. For calculations, the following coefficients were used in the free energy density function (in SI units) [141]: $a_1 = 3.8 \times 10^5$ (T − 479), $a_{11} = -7.3 \times 10^7$, $a_{111} = 2.6 \times 10^8$, $c_{11} = 1.746 \times 10^{11}$, $c_{12} = 7.94 \times 10^{10}$, $q_{11} = 1.203 \times 10^{10}$, $q_{12} = -1.878 \times 10^9$. According to our estimates, $d_{31} = -11 \times 10^{12}$ m/V, $d_{33} = 22 \times 10^{12}$ m/V, $\varepsilon_{33}/\varepsilon_0 = 75$, $P_3 = 1.5$ C/m^2. Experimentally measured piezoelectric coefficient is equal $d_{33} = 25 \times 10^{12}$ m/V [142] that is in agreement with calculated data.

3.1.2. Barium Titanate

In an attempt to calculate the physical parameters of barium titanate using the ferroelectric energy density in the form of Equation (6), we obtained poor estimates that did not match the experimental data. Therefore, the expression for free energy density was expanded to eighth order for modeling the dielectric and piezoelectric parameters of barium titanate as:

$$F_f = a_1P_3^2 + a_{11}P_3^4 + a_{111}P_3^6 + a_{1111}P_3^8 \tag{19}$$

where a_{1111} is the dielectric stiffness coefficient of eighth order. Performing the calculations similar to above enables reducing Equation (5) to the form:

$$F = a_1P_3^2 + b\,P_3^4 + a_{111}P_3^6 + a_{1111}P_3^8 - E_3P_3, \tag{20}$$

where *b* is defined by Equation (12). Based on Equation (13), the equilibrium polarization can be reduced to following form:

$$P_3 = \frac{1}{2\sqrt{3a_{1111}}} \left(r_1 - \frac{3(8\,ba_{1111} - 3a_{111}^2)}{r_1} - 3a_{111} \right)^{1/2} \tag{21}$$

where

$$r_1 = \{108a_{1111}(\, ba_{111} - 2\, a_1 a_{1111}) - 27\, a_{111}{}^3 + 12\sqrt{3}[32\, b^3 a_{1111} - \\ - 9\, b^2 a_{111}{}^2 - 108 a_1 a_{1111}(ba_{111} - a_1 a_{1111}) + 27 a_1 a_{111}^3]^{1/2} a_{1111}\}^{1/3}.$$

Using Equation (15), the piezoelectric coefficients can be derived as:

$$d_{33} = \frac{2P_3(2q_{11}c_{11} - c_{12}q_{11} - 2c_{12}q_{12})}{(c_{11}c_{12} - 2c_{12}{}^2 + c_{11}{}^2)(2a_1 + 12bP_3^2 + 30a_{111}P_3^4 + 56a_{1111}P_3^6)}, \quad (22)$$

$$d_{31} = \frac{2P(-c_{12}q_{11} + c_{11}q_{12})}{(c_{11}c_{12} - 2c_{12}{}^2 + c_{11}{}^2)(2a_1 + 12bP_3^2 + 30a_{111}P_3^4 + 56a_{1111}P_3^6)}, \quad (23)$$

Numerical estimates for dielectric and piezoelectric parameters were carried out at room temperature T = 25 °C. These estimates depend on following coefficients that enter the expression for free energy density [143]: a_1 = 4.124 × 10^5 (T − 115), a_{11} = 5.328 × 10^8, a_{111} = 1.294 × 10^9, a_{1111} = 3.863 × 10^{10}, c_{11} = 1.755 × 10^{11}, c_{12} = 8.464 × 10^{10}, q_{11} = 1.203 × 10^{10}, q_{12} = −1.878 × 10^9. The calculated values are listed below: d_{31} = −37 × 10^{-12} m/V, d_{33} = 95 × 10^{-12} m/V, $\varepsilon_{33}/\varepsilon_0$ = 189, P_3 = 0.26 C/m^2. The obtained estimates are in full agreement with measurement data which were reported recently [144]: d_{31} = −29.4 × 10^{-12} m/V, d_{33} = 86.3 × 10^{-12} m/V, $\varepsilon_{33}/\varepsilon_0$ = 188, P_3 = 0.26 C/m^2.

3.1.3. $LiTaO_3$

$LiNbO_3$ and $LiTaO_3$ belong to the 3*m* point group. Denoting the crystallographic uniaxial directions as the *z*-axis, the free-energy expansion is given as:

$$F = \frac{a_1 P_3^2}{2} + \frac{a_2 P_3^4}{4} + b_1 S_3{}^2 + b_2 (S_1 + S_2)^2 + \\ + b_3((S_1 - S_2)^2 S_6{}^2) + b_4 S_3 (S_1 + S_2) + b_5 (S_4{}^2 + S_5{}^2) + \\ + b_6((S_1 - S_2)S_4 + S_5 S_6) + g_1 (S_1 + S_2) P_3^2 + g_2 S_3 P_3^2 \quad (24)$$

where b_i and g_i are stiffness and electrostriction coefficients. Equilibrium strain components take the form for free sample as:

$$S_4 = 0, \\ S_6 = 0, \\ S_5 = 0, \\ S_2 = \frac{(-2b_1 g_1 + g_2 b_4) P_3^2}{2(b_4{}^2 - 4b_1 b_2)}, \quad (25) \\ S_3 = \frac{(b_4 g_1 + 2g_2 b_2) P_3^2}{b_4{}^2 - 4b_1 b_2}, \\ S_1 = \frac{(-2b_1 g_1 + g_2 b_4) P_3^2}{2(b_4{}^2 - b_1 b_2)}.$$

Substituting Equation (25) into Equation (24) yields:

$$F = a_1 P_3^2 + a_0\, P_3^4, \quad (26)$$

where $a_0 = \frac{a_2 b_4^2 - 4 g_1 g_2 b_4 + 4 b_1 g_1^2 - 4 a_2 b_1 b_2 + 4 b_2 g_2^2}{b_4^2 - 4 b_1 b_2}$.

Equation (26) enables to find the equilibrium polarization:

$$P_3 = \sqrt{\frac{a_1}{a_0}} \tag{27}$$

Then the expressions for piezoelectric coefficients are as follows:

$$\begin{aligned} d_{33} &= -\frac{2P_3(b_4 g_1 - 2 b_2 g_2)}{(b_4{}^2 - 4 b_1 b_2)(-a_1 + 3 a_0 P_3^2)}, \\ d_{31} &= -\frac{(2 b_1 g_1 - b_4 g_2) P_3}{(b_4{}^2 - 4 b_1 b_2)(-a_1 + 3 a_0 P_3^2)}. \end{aligned} \tag{28}$$

For numerical estimation we used the following LGD potential coefficients for $LiTaO_3$: $a_1 = 0.1256 \times 10^{10}$, $b_1 = 0.1355 \times 10^{12}$, $b_2 = 0.6475 \times 10^{11}$, $b_3 = 0.4925 \times 10^{11}$, $b_4 = 0.74 \times 10^{11}$, $b_5 = 0.48 \times 10^{11}$, $b_6 = -0.12 \times 10^{11}$, $g_1 = -0.202 \times 10^9$, $g_2 = 0.1317 \times 10^{10}$, $a_2 = 0.5043 \times 10^{10}$. The calculated values were found to be: $d_{31} = 1.0 \times 10^{-12}$ m/V, $d_{33} = -2.5 \times 10^{-12}$ m/V, $\varepsilon_{33}/\varepsilon_0 = 46$, $P_3 = 0.5$ C/m^2.

3.1.4. $KNbO_3$

To perform the thermodynamic analysis of $KNbO_3$, polarization was assumed to be P = (P_3, 0, P_3) for the rhombohedral phase which is stable at room temperature. In this case, the ferroelectric ordering energy takes the following form under stress-free condition [145-148]:

$$F_f = 2a_1 P_3^2 + (2a_{11} + a_{12}) P_3^4 + 2(a_{111} + a_{112}) P_3^6 + (2a_{1111} + 2a_{1112} + a_{1122}) P_3^8 \tag{29}$$

One can see that Equation (29) is similar to Equation (19) and differs from the latter in renormalized coefficients. Taking this into account, we can calculate the spontaneous polarization components and dielectric susceptibility as:

$$\chi_{ki} = \left(\frac{\partial^2 F}{\partial P_k \, \partial P_i} \right)^{-1} \tag{30}$$

When the cell axis is along the pseudocubic direction, the spontaneous strains can be expressed as:

$$\begin{aligned} S_{11} &= Q_{11} P_1^2 + Q_{12}(P2 + P_3^2); \\ S_{22} &= Q_{11} P_2^2 + Q_{12}(P_1^2 + P_3^2); \\ S_{33} &= Q_{11} P_3^2 + Q_{12}(P_2^2 + P_1^2); \end{aligned} \tag{31}$$

where Q_{11} and Q_{12} are the electrostrictive coefficients. Finally, the piezoelectric coefficients can be found from Equation (15). The energy expansion coefficients used for estimates (in SI units) were as follows: $a_1 = 4.273 \times 10^5 (T - 377)$, $a_{11} = 6.36 \times 10^8$, $a_{12} = 9.66 \times 10^8$, $a_{111} = 2.81 \times 10^9$, $a_{112} = -1.99 \times 10^9$, $a_{123} = 6.03 \times 10^9$, $a_{1111} = 1.74 \times 10^{10}$, $a_{1112} = 5.99 \times 10^9$, $a_{1122} = 2.50 \times 10^{10}$, $a_{1123} = -1.17 \times 10^{10}$, $Q_{11} = 0.12$, $Q_{12} = -0.053$, $Q_{44} = 0.052$. The calculated values are at room temperature were: $P_s = 0.45$ C/m^2, $\varepsilon_{33}/\varepsilon_0 = 55$, $\varepsilon_{22}/\varepsilon_0 = 160$, $\varepsilon_{11}/\varepsilon_0 = 1000$, $d_{31} = 3.4 \times 10^{-12}$ m/V, $d_{32} = -24.3 \times 10^{-12}$ m/V, $d_{33} = 27.4 \times 10^{-12}$ m/V.

Table 2. Dielectric stiffness coefficients used for estimates (in SI units).

Coefficients	**$PbTiO_3$**	**$BaTiO_3$**	**$LiTaO_3$**	**$KNbO_3$**	**$(Na,K)NbO_3$**	**$Na_{0.5}Bi_{0.5}TiO_3$ -$BaTiO_3$**
a_1	3.8×10^5 (T − 479)	4.124×10^5 (T − 115)	1.256×10^9	4.273×10^5 (T − 377)		
a_{11} (a_2)	-7.3×10^7	5.328×10^8	5.043×10^9	6.36×10^8		
a_{12}				9.66×10^8		
a_{111}	2.6×10^8	1.294×10^9		2.81×10^9		
a_{112}				-1.99×10^9		
a_{123}				6.03×10^9		
a_{1111}		3.863×10^{10}		1.74×10^{10}		
a_{1112}				5.99×10^9		
a_{1122}				2.50×10^{10}		
a_{1123}				-1.17×10^{10}		

Table 3. Calculated dielectric and piezoelectric parameters (in SI units).

B	$PbTiO_3$		$BaTiO_3$		$LiTaO_3$		$KNbO_3$		$(Na,K)NbO_3$		$Na_{0.5}Bi_{0.5}TiO_3$ -$BaTiO_3$	
	Theory	Obser-vation	Theory	Obser-vation	Theory	Obser-vation	Theory	Obser-vation	Theory	Obser-vation	Theory	Obser-vation
P_s (C/m^2)	1.5		0.26	0.26	0.5		0.45	0.42				
$\varepsilon_{33}/\varepsilon_0$	75		189	188	46		55					
$\varepsilon_{22}/\varepsilon_0$							160					
$\varepsilon_{11}/\varepsilon_0$							1000					
d_{31} (10^{-12}m/V)	−11		−37	−29.4	1.0		3.4	9.8				
d_{32} (10^{-12}m/V)							−24.3	−22.3				
d_{33} (10^{-12}m/V)	22	25	95	86.3	−2.5		27.4	29.3				

Dielectric stiffness coefficients and calculated dielectric parameters for some piezoelectric materials have been summarized in Tables 2 and 3. One can conclude that substitution of Pb by Ba in $PbTiO_3$ enables higher values of permittivity and piezoelectric coupling coefficients. $LiTaO_3$ and $KNbO_3$ are characterized by weaker piezoelectric coupling. In summary, electrical parameters of lead-based and lead-free piezoelectrics such as the polarization, dielectric permittivity and piezoelectric coefficients can be determined using the Equations (14), (15) and (18) and experimental dielectric stiffness coefficients.

3.2. Theory of Ferroelectric Solid Solutions (Generalized Lattice Model) [149-152]

One of the most common methods for modifying the physical properties is by introduction of some impurities into ferroelectric compounds. Thus, the theoretical and experimental investigations of ferroelectric solid solutions are very attractive. There are a few different approaches to address the problem of theoretically modeling the ferroelectric solid solutions. Most popular approaches are based

on density functional method, quantum chemical calculation and phenomenological thermodynamic models (such as Landau-Ginsburg-Devonshire model). This section contains application of the lattice model to ferroelectric solid solution. This model permits all calculations in analytical form with satisfactory resemblance to experimental data.

Let us consider ferroelectric solid solution as a lattice with two kinds of dipoles distributed over the sites. Suppose the energy of two dipoles located in sites $\mathbf{R}_i$ and $\mathbf{R}_j$ has the following form:

$$U_{ij} = -\sum_{\alpha,\gamma} Q_{\alpha\gamma}(\mathbf{R}_i - \mathbf{R}_j)(\mathbf{D}_\alpha(\mathbf{R}_i)\cdot\mathbf{D}_\gamma(\mathbf{R}_j))n_\alpha(\mathbf{R}_i)n_\gamma(\mathbf{R}_j), \tag{32}$$

where $n_\alpha(\mathbf{R}_i)$ is a dichotomous random variable with values 1 and 0 : it is equal to 1 if site $\mathbf{R}_i$ contains a particle of α -th component, and 0 otherwise.

These variables $n_1(\mathbf{R}_i)$ and $n_2(\mathbf{R}_i)$ obey the relation:

$$n_1(\mathbf{R}_i) + n_2(\mathbf{R}_i) = 1, \tag{33}$$

their mean values are:

$$< n_1(\mathbf{R}_i) >= c_1, \qquad < n_2(\mathbf{R}_i) >= c_2, \qquad c_1 + c_2 = 1 \tag{34}$$

where c_1, c_2 are component's concentrations in the solution.The functions $Q_{\alpha\gamma}(\mathbf{R})$ in lattice models are long-range interaction potentials with cutting on short distances. A system of dipoles in presence of an external electric field $\mathbf{E}$ has the following Hamiltonian:

$$H = -\frac{1}{2}\sum_{i,j}\sum_{\alpha,\gamma} Q_{\alpha\gamma}(\mathbf{R}_i - \mathbf{R}_j)(\mathbf{D}_\alpha(\mathbf{R}_i)\cdot\mathbf{D}_\gamma(\mathbf{R}_j))n_\alpha(\mathbf{R}_i)n_\gamma(\mathbf{R}_j) - \sum_{i,\alpha}(\mathbf{E}\cdot\mathbf{D}_\alpha(\mathbf{R}_i))n_\alpha(\mathbf{R}_i). \tag{35}$$

In self-consistent field approximation for the long-range parts interactions this Hamiltonian can be transformed to following form:

$$H = -\sum_\alpha \left\{ \sum_i (\mathbf{E}_\alpha^{\text{eff}} \cdot \mathbf{D}_\alpha(\mathbf{R}_i)) n_\alpha(\mathbf{R}_i) \right\} = \sum_\alpha \tilde{H}_\alpha^{\text{eff}}, \tag{36}$$

where

$$\mathbf{E}_\alpha^{\text{eff}} = \mathbf{E} + \frac{1}{2} < \sum_{j,\gamma} Q_{\alpha\gamma}(\mathbf{R}_i - \mathbf{R}_j)\mathbf{D}_\gamma(\mathbf{R}_j) n_\gamma(\mathbf{R}_j) > . \tag{37}$$

The second term $\frac{1}{2} < \sum_{j,\gamma} Q_{\alpha\gamma}(\mathbf{R}_i - \mathbf{R}_j)\mathbf{D}_\gamma(\mathbf{R}_j) n_\gamma(\mathbf{R}_j) >$ in this formula is the local effective field due to all the dipoles at point $\mathbf{R}_i$ for dipole of α -th kind (in general case the effective fields for the components are not identical).

3.2.1. Effective Fields

To evaluate Equation (37) one should find the mean values $< n_\gamma(\mathbf{R}_j) >$ under the sum over j, γ sign. In general case these mean values depend on the correlations between component distributions, but in the *effective field approximation* these mean values depend on concentrations of the components:

$$< n_\gamma(\mathbf{R}_j) >= c_\gamma. \tag{38}$$

As a result we have the following expression for effective field

$$\mathbf{E}_{\alpha}^{\text{eff}} = \mathbf{E} + \frac{1}{2}\sum_{\gamma} Q_{\alpha\gamma}^{(0)} < \mathbf{D}_{\gamma} > c_{\gamma}, \tag{39}$$

where

$$Q_{\alpha\gamma}^{(0)} = \sum_{j} Q_{\alpha\gamma}\left(\mathbf{R}_i - \mathbf{R}_j\right) = \sum_{j} Q_{\alpha\gamma}\left(\mathbf{R}_j\right) \tag{40}$$

(the last relation holds by virtue of translation invariance of crystal).

3.2.2. Generating Functional and Polarization of Solution

Generating functional (*i.e*., the partition function a system at an external field presence) in effective field approximation has the following form:

$$Z = \frac{1}{N_1!N_2!}\int\cdots\int\left[\prod_{i,\alpha}\frac{d\Omega_{i,\alpha}}{4\pi}\right]\exp\left[\beta\sum_{i,\alpha}\left(\mathbf{E}_{\alpha}^{\text{eff}}\cdot\mathbf{D}_{\alpha}\left(\mathbf{R}_i\right)\right)n_{\alpha}\left(\mathbf{R}_i\right)\right], \tag{41}$$

where $d\Omega_{i,\alpha}$ is a solid angle infinitesimal element in spherical coordinates $(D_{\alpha},\theta_i,\varphi_i)$

$$d\Omega_{i,\alpha} = \sin\theta_i\, d\theta_i\, d\varphi_i, \tag{42}$$

$\beta = 1/T$, T is absolute temperature in energetic units, N_1 and N_2 are numbers of the dipoles.

The multiple integral (41) is a product of the same type integrals

$$\int\frac{d\Omega}{4\pi}\exp\left[\beta E^{\text{eff}} D\cos\theta\right] = \frac{\sinh\left(\beta E^{\text{eff}} D\right)}{\beta E^{\text{eff}} D}, \tag{43}$$

therefore generating functional in mean field approximation can be evaluated easily

$$Z = \frac{1}{N_1!N_2!}\left[\frac{\sinh\left(\beta E_1^{\text{eff}} D_1\right)}{\beta E_1^{\text{eff}} D_1}\right]^{N_1}\left[\frac{\sinh\left(\beta E_2^{\text{eff}} D_2\right)}{\beta E_2^{\text{eff}} D_2}\right]^{N_2}. \tag{44}$$

Hence we find the system polarization (i.e dipole moment per volume unit) as:

$$P = \frac{1}{V\beta}\frac{\partial\ln Z}{\partial E} = \left\{\frac{N_1}{V}\left[\coth\left(\beta E_1^{\text{eff}} D_1\right) - \frac{1}{\left(\beta E_1^{\text{eff}} D_1\right)}\right]D_1 + \frac{N_2}{V}\left[\coth\left(\beta E_2^{\text{eff}} D_2\right) - \frac{1}{\left(\beta E_2^{\text{eff}} D_2\right)}\right]D_2\right\}. \tag{45}$$

Thus, full polarization of binary solid solution contains two contributions related to both of the components, but these contributions are mutually dependent via the effective fields. Therefore the components contributions into polarization are not additive.

3.2.3. Mean Value of a Single Particle Dipole Moment in Effective Field

Mean value of a single particle dipole moment in external field $\mathbf{E}$ defined as:

$$< D >= \frac{\int e^{-\beta H_1} D\cos\theta\, d\Omega_1}{\int e^{-\beta H_1} d\Omega_1}, \tag{46}$$

and has well known result [153-155]:

$$< D >= DL(\beta DE), \tag{47}$$

where

$$L(z) = \left[\coth(z) - \frac{1}{z} \right] \tag{48}$$

is the Langevin function, H_1 is the Hamiltonian of single dipole with moment $\mathbf{D}$ in external field $\mathbf{E}$

$$H_1 = -(\mathbf{E} \cdot \mathbf{D}). \tag{49}$$

For one-component the system of expressions (37) has a simple form

$$\mathbf{E}^{\text{eff}} = \mathbf{E} + \frac{1}{2} Q^{(0)} < \mathbf{D} >, \tag{50}$$

Substitution $\mathbf{E}^{\text{eff}}$ instead of $\mathbf{E}$ into formula (43) leads to transcendent equation with respect to $< D >$. It is well known this equation has a nontrivial solution $< D > \neq 0$ at $T < T_c$.

3.2.4. Polarization of Solid Solution

System of equations for mean values $< D_1 >$ and $< D_2 >$ of dipole moments of the solution components follows from relation (45):

$$\begin{cases} < D_1 >= D_1 \left[\coth\left(\beta D_1 \left\{ E + \frac{1}{2} \sum_\gamma Q_{1\gamma}^{(0)} < D_\gamma > c_\gamma \right\} \right) - \frac{1}{\beta D_1 \left\{ E + \frac{1}{2} \sum_\gamma Q_{1\gamma}^{(0)} < D_\gamma > c_\gamma \right\}} \right] \\ < D_2 >= D_2 \left[\coth\left(\beta D_2 \left\{ E + \frac{1}{2} \sum_\gamma Q_{2\gamma}^{(0)} < D_\gamma > c_\gamma \right\} \right) - \frac{1}{\beta D_2 \left\{ E + \frac{1}{2} \sum_\gamma Q_{2\gamma}^{(0)} < D_\gamma > c_\gamma \right\}} \right]. \end{cases} \tag{51}$$

Note the connection between $< D_1 >$ and $< D_2 >$ realize via non-diagonal elements of matrix $Q_{\alpha\gamma}^{(0)}$ only. It is clear that the solution $\{< D_1 >, < D_2 >\}$ of this system of equations depends on the temperature, the external field, and all of the matrix elements $Q_{\alpha\gamma}^{(0)}$. To solve this system we should know the parameters of the physical system, *i.e.*, matrix elements $Q_{\alpha\gamma}^{(0)}$. These elements should be find using some experimental data.

Solution of system (51) with respect to $< D_1 >$, $< D_2 >$ permits to find polarization of the system as function of external field E

$$P = \frac{N}{V} [c_1 < D_1 > + c_2 < D_2 >] \tag{52}$$

and consequently the susceptibility χ of this system:

$$\chi = \frac{N}{V} \left[c_1 \frac{\partial < D_1 >}{\partial E} + c_2 \frac{\partial < D_2 >}{\partial E} \right] \tag{53}$$

The Langevin function $L(z)$ contains two terms. The first term is a transcendent function, the second is an algebraic function. Both of them have a singularity at $z = 0$. These circumstances complicate search of the solution. Therefore, the Langevin function should be approximated by some more suitable function with correct asymptotic behavior at $z \to 0$ and $z \to \infty$. In the capacity of such approximation we shall use the following function

$$L(z) \approx \frac{2}{\pi} \arctan\left(\frac{\pi z}{6}\right). \tag{54}$$

Note, this approximation is well not only for the Langevin function, but also for its derivative

$$L'(z) \approx \frac{12}{36 + \pi^2 z^2}. \tag{55}$$

This approximation for the Langevin function permits to simplify the system of Equations (51)

$$< D_\alpha >= \frac{2D_\alpha}{\pi} \arctan\left(\frac{\pi\beta D_\alpha}{6}\left[E + \frac{1}{2}\sum_\gamma Q_{\alpha\gamma}^{(0)} < D_\gamma > c_\gamma\right]\right), \qquad (\alpha = 1,2). \tag{56}$$

3.2.5. Parameters of the Components

Some of the parameters D_α and $Q_{\alpha\alpha}^{(0)}$ of solution can be find from experimental data of the components. Equation (56) for a pure component ($c_\alpha = 1, c_\gamma\big|_{\gamma \neq \alpha} = 0$) have the following form

$$< D_\alpha >= \frac{2D_\alpha}{\pi} \arctan\left(\frac{\pi\beta D_\alpha}{6}\left\{E + \frac{1}{2} Q_{\alpha\alpha}^{(0)} < D_\alpha >\right\}\right). \tag{57}$$

This equation describes connection between external field E and mean value of dipole moment D_α. Critical temperature can find from condition existence of nontrivial solution (*i.e.*, $< D_\alpha > \neq 0$) in external field vanishing $E = 0$. Graphical analysis of Equation (57) leads to following connection between critical temperature T_c^α and the model parameters

$$\frac{(D_\alpha)^2 Q_{\alpha\alpha}^{(0)}}{6} = T_c^\alpha. \tag{58}$$

Differentiating both of sides of Equation (57) with respect to E

$$\frac{\partial < D_\alpha >}{\partial E} = \frac{12\beta (D_\alpha)^2}{36 + (\pi\beta D_\alpha)^2\left[E + \frac{1}{2} Q_{\alpha\alpha}^{(0)} < D_\alpha >\right]^2}\left(1 + \frac{1}{2} Q_{\alpha\alpha}^{(0)} \frac{\partial < D_\alpha >}{\partial E}\right), \tag{59}$$

we find derivate

$$\frac{\partial < D_\alpha >}{\partial E} = \frac{12\beta (D_\alpha)^2}{\left[36 + (\pi\beta D_\alpha)^2\left[E + \frac{1}{2} Q_{\alpha\alpha}^{(0)} < D_\alpha >\right]^2\right] - 6\beta Q_{\alpha\alpha}^{(0)} (D_\alpha)^2}. \tag{60}$$

Eliminating $Q_{\alpha\alpha}^{(0)}$ from the last equation with account (58), we obtain susceptibility of the pure ferroelectrics:

$$\chi = \frac{N_\alpha}{V}\frac{\partial < D_\alpha >}{\partial E} = \frac{N_\alpha}{V}\frac{12\beta(D_\alpha)^2}{\left\{36\left(1-\frac{T_c}{T}\right)+\left(\frac{\pi}{T}\right)^2\left[ED+3T_c\frac{< D_\alpha >}{D_\alpha}\right]^2\right\}}. \quad (61)$$

At $E = 0$ the susceptibility have a singularity in vicinity of the critical point T_c.

3.2.6. Susceptibility of Solid Solution

After differentiating both sides of each equation in (56) over E we obtain a system of linear algebraic equations for $\frac{\partial < D_\alpha >}{\partial E}$:

$$\frac{\partial < D_\alpha >}{\partial E} = \frac{12\beta(D_\alpha)^2}{36+(\pi\beta D_\alpha)^2\left[E+\frac{1}{2}\sum_\gamma Q^{(0)}_{\alpha\gamma}c_\gamma < D_\gamma >\right]^2}\left(1+\frac{1}{2}\sum_\gamma Q^{(0)}_{\alpha\gamma}c_\gamma\frac{\partial < D_\gamma >}{\partial E}\right). \quad (62)$$

This system have the following short form:

$$\begin{cases}(1-A_1B_{11})\frac{\partial < D_1 >}{\partial E}-A_1B_{12}\frac{\partial < D_2 >}{\partial E}=A_1;\\ -A_2B_{21}\frac{\partial < D_1 >}{\partial E}+(1-A_2B_{22})\frac{\partial < D_2 >}{\partial E}=A_2,\end{cases} \quad (63)$$

where

$$A_\alpha = \frac{12\beta(D_\alpha)^2}{36+(\pi\beta D_\alpha)^2\left[E+\frac{1}{2}\sum_\gamma Q^{(0)}_{\alpha\gamma}c_\gamma < D_\gamma >\right]^2}, \quad (64)$$

and

$$B_{\alpha\gamma} = \frac{1}{2}Q^{(0)}_{\alpha\gamma}c_\gamma. \quad (65)$$

Hence we have for $\frac{\partial < D_1 >}{\partial E}$ and $\frac{\partial < D_2 >}{\partial E}$:

$$\begin{cases}\frac{\partial < D_1 >}{\partial E}=\frac{A_1(1-A_2B_{22}+A_2B_{12})}{1-A_1B_{11}-A_2B_{22}+A_1A_2[B_{11}B_{22}-B_{12}B_{21}]},\\ \frac{\partial < D_2 >}{\partial E}=\frac{A_2(1-A_1B_{11}+A_1B_{21})}{1-A_1B_{11}-A_2B_{22}+A_1A_2[B_{11}B_{22}-B_{12}B_{21}]}.\end{cases} \quad (66)$$

This system of equations will be used for the critical point finding.

3.2.7. Critical Points of Solid Solutions and Model Parameters

The solution susceptibility (53) in the critical point has a singularity due to vanishing denominators in right hand sides of (66)

$$1-A_1B_{11}-A_2B_{22}+A_1A_2[B_{11}B_{22}-B_{12}B_{21}]=0. \quad (67)$$

This equation takes place under the conditions

$$\begin{cases} E = 0; \\ < D_1 >=< D_1 >= 0. \end{cases} \tag{68}$$

The second of these conditions due to the polarization vanishing at $T > T_c$.

Substituting expressions (64) and (65) with conditions (68) account into Equation (67), we obtain the quadratic equation with respect to critical temperature T

$$T^2 - \frac{(D_1)^2 Q_{11}^{(0)} c_1 + (D_2)^2 Q_{22}^{(0)} c_2}{6} T + \frac{c_1 c_2}{36} (D_1)^2 (D_2)^2 \left[Q_{11}^{(0)} Q_{22}^{(0)} - Q_{12}^{(0)} Q_{21}^{(0)} \right] = 0. \tag{69}$$

Discriminant of this equation in relation to symmetry property of the matrix $Q_{\alpha\gamma}^{(0)}$ is non-negative

$$\widetilde{D} = \left[(D_1)^2 Q_{11}^{(0)} c_1 - (D_2)^2 Q_{22}^{(0)} c_2 \right]^2 + 4 c_1 c_2 (D_1)^2 (D_2)^2 Q_{12}^{(0)} Q_{11}^{(0)} \geq 0, \tag{70}$$

therefore this equation has two real solutions.

Two variants are possible depending on the quantity Q sign

$$Q = Q_{11}^{(0)} Q_{22}^{(0)} - Q_{12}^{(0)} Q_{21}^{(0)}. \tag{71}$$

• $Q \leq 0$. In this case one of the solutions is positive, and the second solution is negative. The positive solution has a physical sense as the Curie temperature, the negative solution has not any physical sense.

• $Q > 0$. In this case both of the solutions are positive. A physical interpretation of this case can be clarified after temperature analysis of the Equations (56)'s solutions. Thus, at condition $Q > 0$ two-component ferroelectric solid solution has two critical points.

Note that the critical points of solutions depends on such combinations dipole moments D_α and interatomic potentials $Q_{\alpha\gamma}^{(0)}$

$$G_{\alpha\gamma} = Q_{\alpha\gamma}^{(0)} D_\alpha D_\gamma. \tag{72}$$

Transform the equation (65) using these combinations

$$T^2 - \frac{G_{11}(1-x) + G_{22} x}{6} T + \frac{x(1-x)}{36} \left[G_{11} G_{22} - G_{12} G_{21} \right] = 0, \tag{73}$$

where $x = c_2$ is second component concentration, $c_1 = 1 - x$.

Let us introduce a new parameter

$$G = G_{11} G_{22} - G_{12} G_{21} \tag{74}$$

and consider a general way of the model parameters G_{11}, G_{22}, G finding by the method of least squares.

Let us introduce the function $f(G, G_{11}, G_{22}, T, x)$

$$f(G, G_{11}, G_{22}, T, x) = T^2 - \frac{G_{11}(1-x) + G_{22} x}{6} T + \frac{x(1-x)}{36} G \tag{75}$$

and find the parameters G, G_{11}, G_{22} by means of the function $F(G, G_{11}, G_{22})$ minimization:

$$F(G, G_{11}, G_{22}) = \sum_i f^2 (G, G_{11}, G_{22}, T_i, x_i) = \min, \tag{76}$$

where T_i, x_i are the experimental points. As a result, system of equations for the model parameters G, G_{11}, G_{22} finding has the following form:

$$\begin{cases} \dfrac{\partial F(G, G_{11}, G_{22})}{\partial G} = 0; \\ \dfrac{\partial F(G, G_{11}, G_{22})}{\partial G_{11}} = 0; \\ \dfrac{\partial F(G, G_{11}, G_{22})}{\partial G_{22}} = 0. \end{cases} \tag{77}$$

After parameters G, G_{11}, G_{22} finding it is possible to perform research of the Curie temperature as function of solution composition.

3.2.8. System $Ba_{1-x}Pb_xTiO_3$

There are the experimental data for Curie temperature of the system $Ba_{1-x}Pb_xTiO_3$ at concentrations $0 \le x \le 1$ [153-157]. The part of the measurement results presented in the Table 4.

Table 4. Curie temperatures as a function of composition of $Ba_{1-x}Pb_xTiO_3$.

x	0	0.5	1.0
T(x)	393 K	623 K	763 K

The first line contains the concentration of $PbTiO_3$ in the system, the second line contains the corresponding Curie temperatures. Results of the parameters G_{11}, G_{22}, G calculations are:

$$\begin{cases} G_{11} = 2358 \text{ K} \\ G_{22} = 4578 \text{ K}; \\ G = -4.043 \cdot 10^6 \text{ K}^2. \end{cases} \tag{78}$$

Results of these parameters using Curie temperatures of the solutions are presented in Figure 6. These results are in close agreement with experimental data.

Figure 6. Calculated dependence of the Curie temperature of the system $Ba_{1-x}Pb_xTiO_3$.

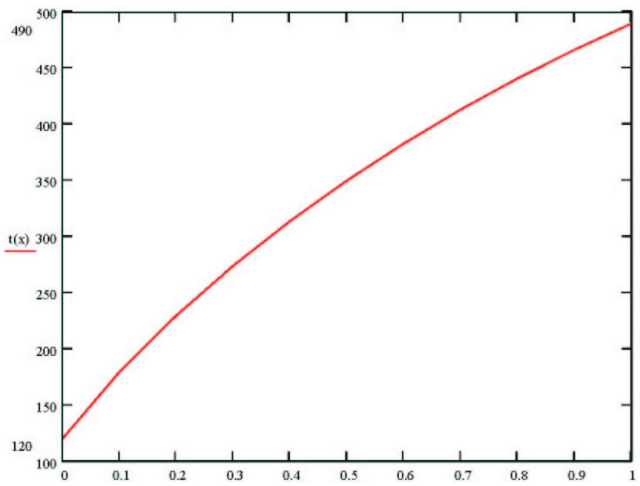

Thus, the lattice model with effective field approximation for long-range parts of the interatomic potentials can be used for description of the ferroelectric solid solutions. But, the essential restriction of the model should be noted: this approach in the present form can be realized in the case of similarity of the crystal structures of the solid solution components only. Otherwise the method should be modified.

4. Modeling of Magnetoelectric Composites

The theory for 3-0 composites is based on the cubic model of composite [158,159]. The sample is assumed to consist of cubes. Dimensions of sample are supposed to be small compared with wave-lengths of AC fields used in the measurements. One, therefore, needs to obviously analyze only one of the units to describe the whole sample. For a unit cube, Equations (79) and (80) are described. The boundary conditions consist in force balance and equality of medium displacement on the boundaries. Using Equations (79) and (80) and boundary conditions enables one to obtain ME voltage coefficient numerically. Calculations show that the peak longitudinal ME voltage coefficient for 3-0 connectivity reaches 4000 mV/cm Oe and is three times higher than the transverse coefficient when the poling direction is perpendicular to the bias magnetic field. In case of 0-3 connectivity the peak longitudinal ME voltage coefficient equals 900 mV/cm Oe. In a real composite sample, the internal units are clamped by neighboring ones. Taking into account the clamping effect caused by surrounding unites cubes leads to significant decreasing of ME voltage coefficients.

PZT volume fraction dependence of transverse ME voltage coefficients is shown in Figure 7 for the sample in which internal units are assumed to be clamped by neighboring ones.

Figure 7. Piezoelectric volume fraction dependence of ME voltage coefficient for 3–0 and 0–3 composites of NZFO-PZT and NZFO-KNNBT.

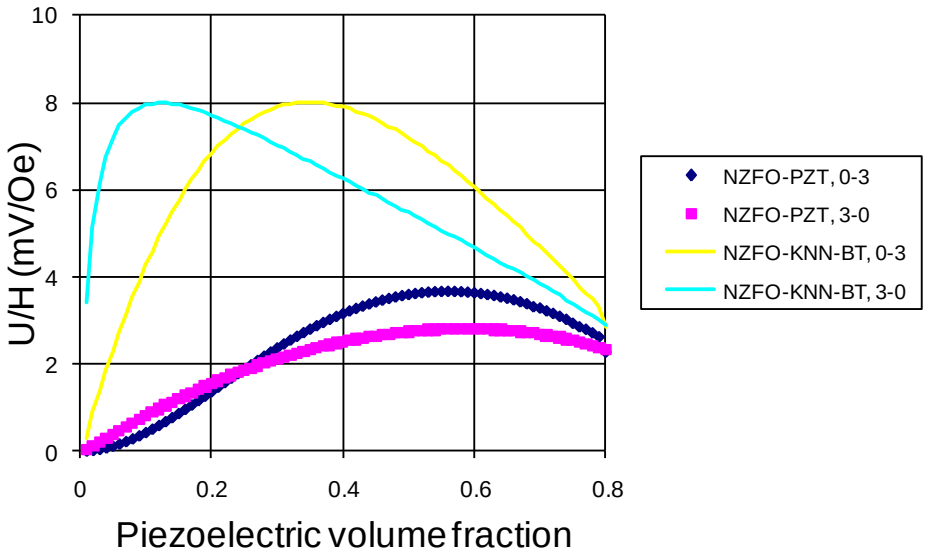

Further, we consider only symmetric extensional deformation in this model and ignore any asymmetric flexural deformations of the layers that would lead to a complex solving procedure. Our

consideration is based on the following equations that can be written for the polarized piezoelectric phase with the symmetry ∞m for the strain and electric displacement:

$$\begin{aligned} {}^{p}S_i &= {}^{p}s_{ij}\,{}^{p}T_j + {}^{p}d_{ki}\,{}^{p}E_k \\ {}^{p}D_k &= {}^{p}d_{ki}\,{}^{p}T_i + {}^{p}\varepsilon_{kn}\,{}^{p}E_n \end{aligned} \tag{79}$$

where ${}^{p}S_i$ and ${}^{p}T_j$ are strain and stress tensor components of the piezoelectric phase, ${}^{p}E_k$ and ${}^{p}D_k$ are the vector components of electric field and electric displacement, ${}^{p}s_{ij}$ and ${}^{p}d_{ki}$ are compliance and piezoelectric coefficients, and ${}^{p}\varepsilon_{kn}$ is the permittivity matrix.

The magnetostrictive phase is assumed to have a cubic symmetry and is described by the equations:

$${}^{m}S_i = {}^{m}s_{ij}\,{}^{m}T_j + {}^{m}q_{ki}\,{}^{m}H_k \tag{80}$$

where ${}^{m}S_i$ and ${}^{m}T_j$ are strain and stress tensor components of the magnetostrictive phase, ${}^{m}H_k$ and are the vector components of magnetic field, ${}^{m}s_{ij}$ and ${}^{m}q_{ki}$ are compliance and piezomagnetic coefficients.

The layers are assumed to be perfectly coupled at the interface and we use the following boundary conditions:

$$v\,{}^{p}T_i + (1 - v){}^{m}T_i = 0 \text{ and } {}^{p}S_i = {}^{m}S_i \text{ for } i=1, 2, \tag{81}$$

where v is PZT volume fraction.

Equations (79)–(81) yield the expression for ME voltage coefficient for longitudinal fields' orientation as:

$$\begin{aligned} \alpha_{E\,33} = \frac{E_3}{H_3} = 2\frac{\mu_0 v(1-v)\,{}^{p}d_{31}\,{}^{m}q_{31}}{\{2\,{}^{p}d_{31}^2(1-v) + {}^{p}\varepsilon_{33}[({}^{p}s_{11} + {}^{p}s_{12})(v-1) - v({}^{m}s_{11} + {}^{m}s_{12})]\}} \\ \times\frac{[({}^{p}s_{11} + {}^{p}s_{12})(v-1) - v({}^{m}s_{11} + {}^{m}s_{12})]}{\{[\mu_0(v-1) - {}^{m}\mu_{33}v][v({}^{m}s_{12} + {}^{m}s_{11}) - ({}^{p}s_{11} + {}^{p}s_{12})(v-1)] + 2\,{}^{m}q_{31}^2 v^2\}} \end{aligned} \tag{82}$$

where E_k and H_k are vector components of the electric and magnetic field; s_{ij} is an compliance coefficient; d_{ki} is a piezoelectric coefficient; q_{ki} is a piezomagnetic coefficient; ε_{kn} is permittivity.

For transverse fields' orientation, the following expression can be obtained for ME voltage coefficient:

$$\alpha_{E,31} = \frac{E_3}{H_1} = \frac{-v(1-v)({}^{m}q_{11} + {}^{m}q_{21})\,{}^{p}d_{31}}{{}^{p}\varepsilon_{33}({}^{m}s_{12} + {}^{m}s_{11})v + {}^{p}\varepsilon_{33}({}^{p}s_{11} + {}^{p}s_{12})(1-v) - 2\,{}^{p}d_{31}^2(1-v)} \tag{83}$$

As an example, numerical estimates are made for bilayers of NZFO, cobalt freite (CFO) or Ni and PZT or lead-free ferroelectrics. Using the zinc-substituted nickel ferrite is dictated by fact that when Zn is substituted in nickel ferrite, the room temperature q varies linearly with increasing Zn concentration x for $x < 0.3$ [160]. The material parameters used for theoretical estimates are listed in Table 5. Calculations of magnetically induced voltage are for the sample thickness of 1 mm.

Table 5. Material parameters (compliance coefficient s, piezomagnetic coupling q, piezoelectric coefficient d, and permittivity ε) for NZFO, CFO, Ni, PZT and lead-free ferroelectrics [161,162] used for theoretical estimates.

Material	s_{11} (10^{-12} m^2/N)	s_{12} (10^{-12} m^2/N)	q_{11} (10^{-12} m/A)	q_{12} (10^{-12} m/A)	d_{31} (10^{-12} m/V)	d_{33} (10^{-12} m/V)	$\varepsilon_{33}/\varepsilon_0$
PZT	17.3	−7.22	-	-	−175	400	1750
NBT-BT	7.3	−3.2	-	-	−140	280	2000
Mn:NBT-BT	7.3	−3.2			−242	483	4000
NKN-BT	5.55	−1.04			−110	225	1058
NZFO	6.5	−2.4	−1050	210			-
CFO	6.5	−2.4	−1880	556			
Ni	4.9	−1.5	−4140	570			

Figure 8 shows the piezoelectric volume fraction dependence of ME voltage coefficient for NZFO-PZT, NZFO-MBT-BT, NZFO-Mn:MBT-BT, and NZFO-NKN-BT and for CFO-PZT, CFO-MBT-BT, CFO-Mn:MBT-BT, and CFO-NKN-BT for longitudinal fields' orientation.

One can see from Figures 8 and 9 that the transverse ME voltage coefficient considerably exceeds the longitudinal one that is attributed to a reduction in the internal magnetic field due to finite magnetic permeability of ferrite and demagnetizing fields for longitudinal fields' orientation. The stronger piezomagnetic coupling for CFO (see Table 5) results in increased ME coefficients compared to NZFO. Figures 10 and 11 show the futher increase of ME effect at the replacement of ferrites by a Ni phase.

Figure 8. Piezoelectric volume fraction dependence of longitudinal magnetoelectric (ME) voltage coefficient for bilayers of NZFO and piezoelectrics **(a)** and CFO and piezoelectrics **(b)**.

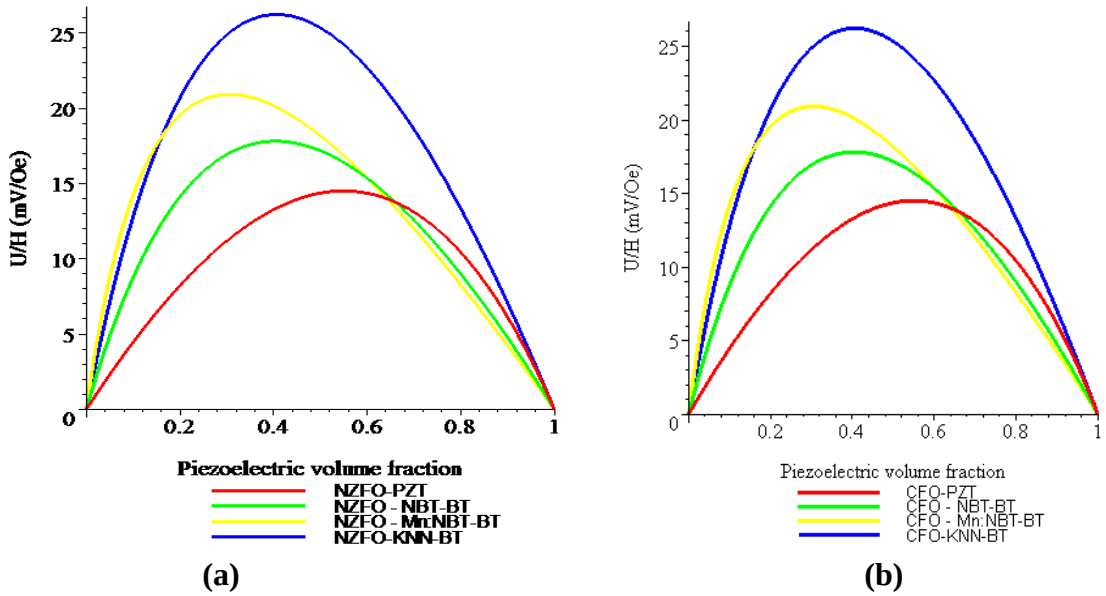

(a) **(b)**

Figure 9. Piezoelectric volume fraction dependence of transverse ME voltage coefficient for bilayers of NZFO and piezoelectrics **(a)** and CFO and piezoelectrics **(b)**.

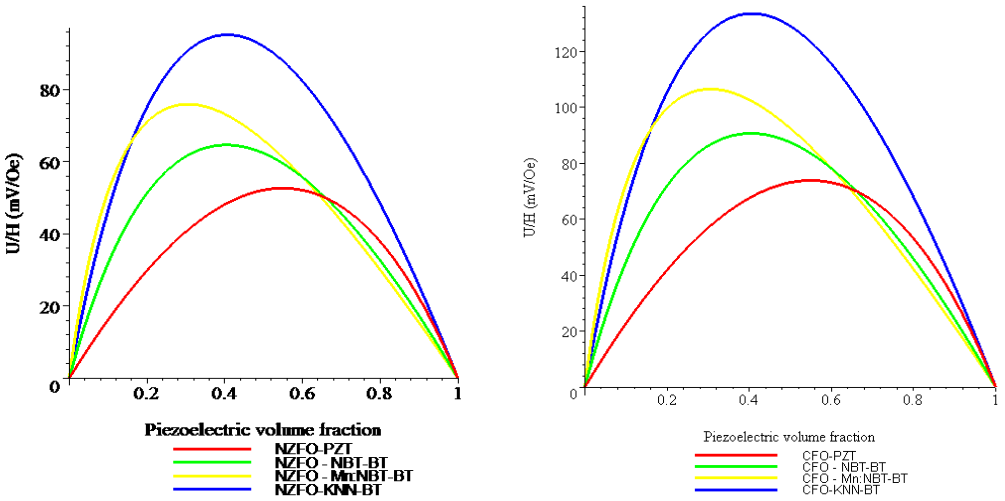

(a) **(b)**

Figure 10. Piezoelectric volume fraction dependence of longitudinal ME voltage coefficient for a bilayer of Ni and piezoelectrics.

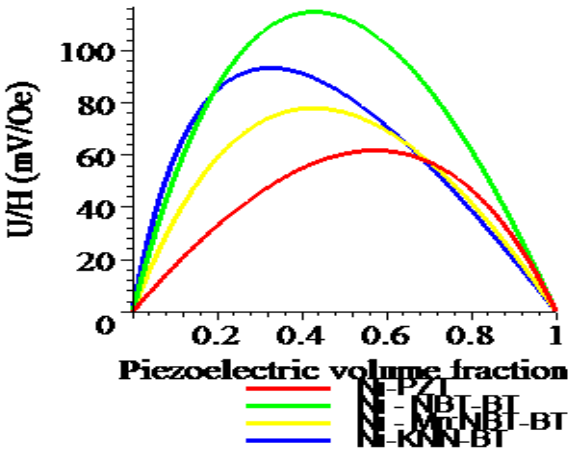

Figure 11. Piezoelectric volume fraction dependence of transverse ME voltage coefficient for a bilayer of Ni and piezoelectrics.

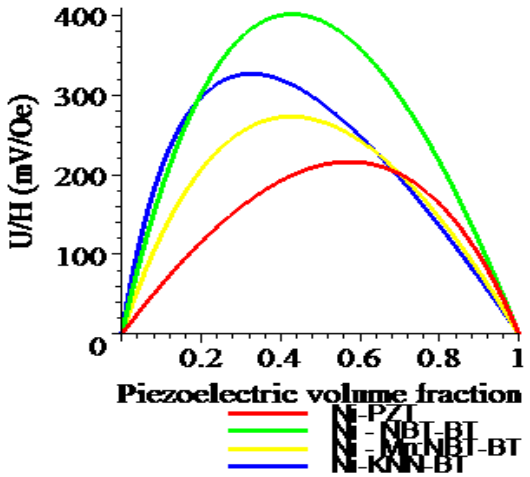

The above theory is for samples that are free of any external mechanical force. Now we consider bilayers that are clamped perpendicular to the plane of the bilayer, along direction 3. The compliance of the clamp system is represented by s_{c33}, with zero compliance for rigidly clamped samples and infinite compliance for unclamped samples. As an example, we consider ME coupling in a clamped bilayer for transverse field orientation. The boundary conditions for the clamped sample become $T1 = 0$, $T2 = 0$, and $T3 = s_{c33}\ T_3$. The transverse ME voltage coefficient is determined by the expression (84)

$$\alpha_{E,31} = \frac{\alpha_{31}(s_{33}+s_{c33})-d_{33}q_{33}}{\varepsilon_{33}(s_{33}+s_{c33})-d_{33}^2} \quad (84)$$

where α_{33}, s_{33}, d_{33}, q_{33}, and ε_{33} are ME susceptibility, effective compliance, piezoelectric and piezomagnetic coefficients, and permittivity of composite [8]. The numerical estimate of ME coupling is presented in Figure 12 for free and rigidly clamped bilayers of PZT and NZFO. One can see from Figure 12 that clamping the sample reduced ME coupling by half.

Figure 12. PZT volume fraction dependence of ME voltage coefficient for free and rigidly clamped bilayers of NZFO and PZT for transverse fields' orientation.

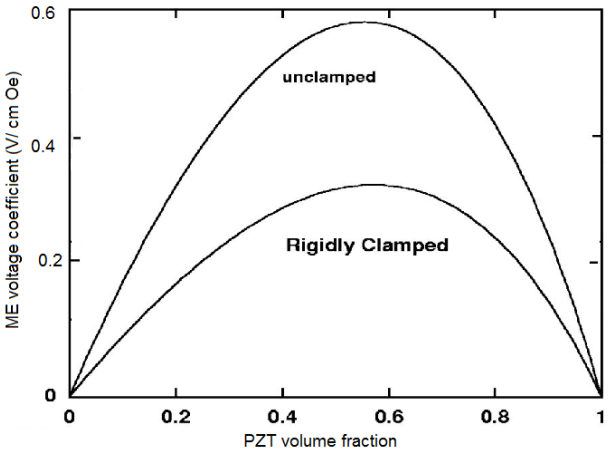

5. Data on Magnetoelectric Response in 3-0, 2-2, and 1-3 Composites

5.1. ME Effect in Sintered Composites

Magnetoelectric composite materials consisting of piezoelectric and magnetostrictive phases respond to both electric and magnetic field. The composites exploit product property and various synthesis techniques can be adopted to combine two different phases depending upon the crystal symmetry, lattice parameters and physical state. The presence of piezoelectric and magnetostrictive phases in the same material provides the opportunity to develop a voltage gain device operating on the following principle. An applied AC magnetic field induces strain in the magnetostrictive phase which is transferred onto the piezoelectric phase in an elastically coupled system. The piezoelectric phase produces the electric charge in proportion to the applied strain. Figure 13 summarizes the magnitude of ME coefficient reported for *in situ* and particulate sintered composites [12,24,163-166]. It can be immediately noticed that multi-layer laminates with inter-digital electrodes provide the highest

magnitude of ME coefficient. Figure 13 also shows the interface microstructure in $Pb(Zr,Ti)O_3$-$(Ni,Zn)Fe_2O_4$ (PZT-NZF) composites with bilayer geometry with no intermediate electrodes. By tuning the concentration of ionic dopants it is possible to achieve dense interfacial structures which can compensate for the lattice mismatch between the perovskite and spinel. However, diffusion of Zn and Cu ions into piezoelectric phase and Pb ions into magnetostrictive phase limits the magnitude of maximum achievable ME coupling. The diffusion length in Figure 13 is of the order of 15–20 μm with synthesis temperatures in the range of 1100 ℃. In particulate composites there is additional problem limiting the magnitude of ME coupling, namely 3D connectivity of magnetic phase which for smaller piezoelectric grain sizes can be noticeable. It is now well understood that ME coefficient in particulate composites can be tailored to their maximum magnitude by synthesizing high piezoelectric voltage coefficient "g" and high piezoelectric strain coefficient "d" phase surrounded by low magnetic coercivity and high magnetization magnetostrictive phase. Additional constraint is imposed by the equivalence of mechanical impedance.

Figure 13. Magnetoelectric coefficient for various bulk sintered composites.

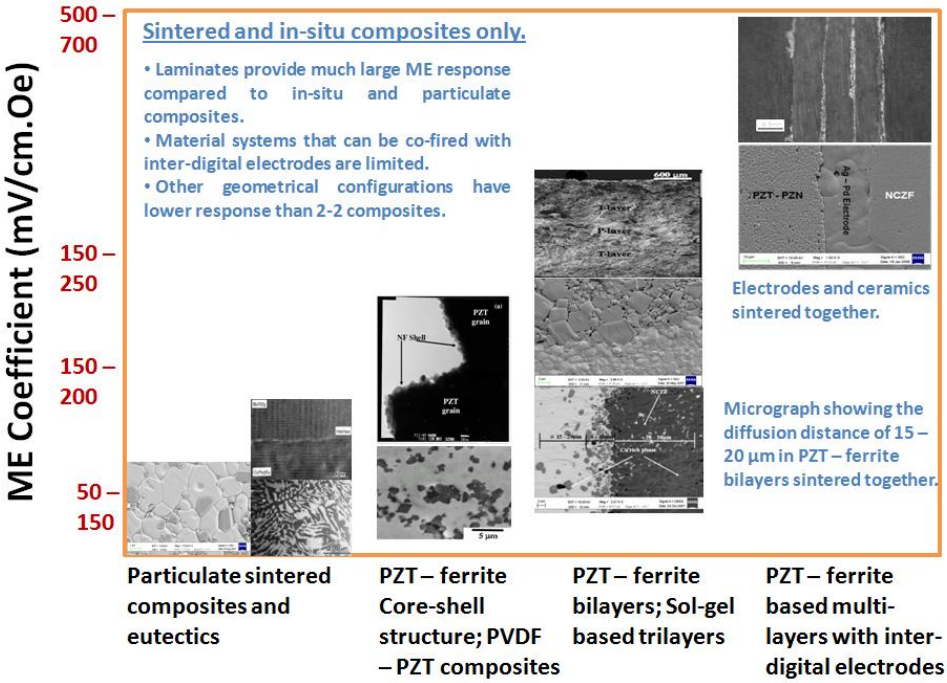

Figure 14(a) and (b) shows the variations in ME coupling with varying piezoelectric grain size in 3–0 particulate $Pb(Zr_{0.52}Ti_{0.48})O_3$ (PZT)-$Ni_{0.8}Zn_{0.2}Fe_2O_4$ (NZF) composites [167]. It was found that as the piezoelectric phase grain size increases the overall resistivity, piezoelectric, dielectric and ferroelectric property of the composite increases and saturates above 600 nm. Below 200 nm average grain size, piezoelectric and dielectric properties decrease rapidly. The size effect of magnetic phase was small. In addition to diffusion, the main problem limiting the magnitude of ME coupling was found to be 3D connectivity of the magnetic phase, which for smaller piezoelectric grain sizes can be noticeable.

Figure 14. Magnetoelectric responses as a function of **(a)** DC bias field and **(b)** grain size of PZT.

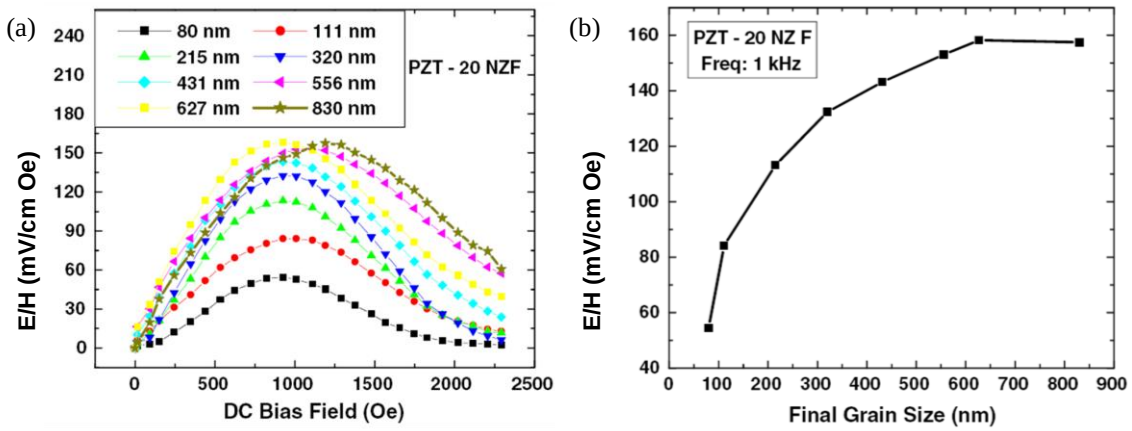

In layered composites the connectivity is limited to the region near the interface. For thin film systems, this may form the significant fraction of the overall system. Self-assembled microstructures (such as eutectic decomposition and strain minimization) suffer from the drawback that ferroelectric polarization is reduced in the system due to formation of mechanical twins, thus exhibiting low magnitude of ME coupling. $BaTiO_3$-$CoFe_2O_4$ (BTO-CFO) system particulate composite with eutectic composition were reported by Echigoya *et al*. [163]. Even though the phase distribution occurs with high periodicity and interface exhibits crystallographic orientation relationships, the magnitude of ME coupling remains low. The orientation relationships between phases in eutectic decomposition of BTO-CFO can be expressed as: (i) for hcp $BaTiO_3$: (111)CFO//(00.1)BTO and (110)CFO//(11.0)BTO; and (ii) for tetra/cubic $BaTiO_3$: (001)CFO//(001)BTO and (100)CFO//(100) BTO.

High magnetostrictive coefficients are obtained in the compounds of the type R–T where R is rare earth and T is the transition metal, however these materials have poor resistivity and are chemically reactive. Thus, the choice for the magnetostrictive phase in grown / sintered composites narrows down to the spinel ferrites. In the spinel ferrites, the spontaneous magnetization corresponds to the difference between the sublattice magnetizations associated with the octahedral and tetrahedral sites. Results have shown enhanced magnitude of the ME coefficient for $Ni_{0.8}Zn_{0.2}Fe_2O_4$ (NZF) and $Co_{0.6}Zn_{0.4}Fe_2O_4$ (CZF). In the nickel zinc ferrite solid solution ($Ni_{1-x}Zn_xFe_2O_4$) as x is increased Zn^{2+} replaces Fe^{3+} in the tetrahedral sites and Fe^{3+} fills the octahedral sites emptied by Ni^{2+}. The net magnetization of nickel zinc ferrite is proportional to $5(1 + x) + 2(1 - x) - 0(x) - 5(1 - x) = 2 + 8x$. Thus, the magnetic moment as a function of the Zn content increases until there are so few Fe^{3+} ions remaining in tetrahedral sites that the superexchange coupling between tetrahedral and octahedral sites breaks down. Figure 15 shows our results on the PZT-NZF and PZT-CZF composites. It can be seen from this figure that CZF is a hard magnetic phase, requires higher DC bias, has lower remanent magnetization and results in larger reduction of the ferroelectric polarization as compared to NZF. On the other hand, a high increase in the resistivity of the Ni-ferrites is obtained by doping with Co. Further, the sintering of Ni-ferrites has been found to be simpler with the PZT matrix due to low temperatures and adequate grain growth.

Figure 15. Comparison of magnetic properties for PZT-NZF and PZT-CZF.

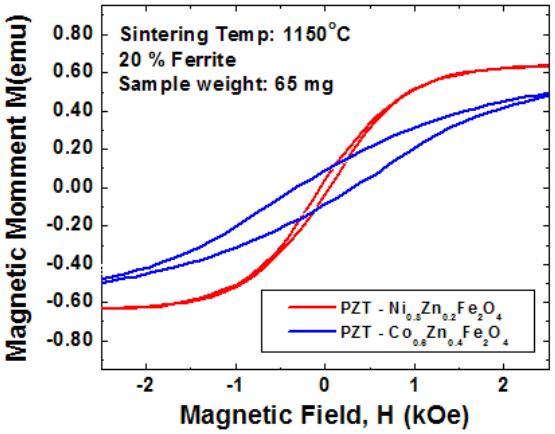

In particulate-sintered composites consisting of random distribution of magnetostrictive particles, there is excessive cross-diffusion of ions across the interface. Recently, it was shown in Cu-modified nickel zinc ferrite (NCZF)–PZNT composites that Cu ions diffuse into PZNT while Pb ions diffuse into NCZF. This cross-diffusion lowers the magnitude of magnetostrictive constant and piezoelectric voltage constant. Another drawback of particulate-sintered composites is connectivity of the ferrite particles which lowers the overall resistivity and reduces the poling voltage. However, by confining the distribution of NFO along the grain boundaries and controlling the fraction of such boundaries, higher poling voltage can be applied. Figure 16(a) and (b) shows the simulation of the magnetic field pattern when the ferrite particles and ferrite plates are placed in between the strong DC magnetic field. The magnetic field pattern clearly reveals that the plates are able to reach the saturation state for a given applied magnetic field while dispersed particle do not because the flux line originating from the particles shield the response. This data provides another explanation for the experimentally observed fact that magnetoelectric response of the sintered *in situ* composites is lower than the layered ones. The field in textured nanocomposite can be enhanced by coupling with the external layers.

Recent results by Grossinger *et al*. on composite consisting of 50% cobalt ferrite-50% barium titanate in core-shell structure show giant increase in ME coefficient as compared to randomly dispersed composites [168]. The results were analyzed in terms of coupling coefficient k, given as $k_{par} = \lambda_{par} d\lambda_{par}/dH$, where λ_{par} represents the longitudinal magnetostriction, H is the applied magnetic field, and d is the effective sample thickness. It was shown that the magnitude of ME coefficient increases with k which is higher for core-shell structure. These results are consistent with our own data which shows that core-shell $Pb(Zr,Ti)O_3$ (PZT)-$NiFe_2O_4$ (NFO) particulate nanocomposites provide higher magnitude of ME coefficient. In our case, core-shell composites were synthesized through high pressure sintering which resulted in good interface bonding and effective strain transfer across the interface [169]. The microstructure in Figure 17, which has a resemblance to core-shell structure, can provide effective elastic coupling between the magnetostrictive and piezoelectric phases. The magnitude of magnetostriction coefficient, λ_{par}, and k will be higher for the NFO-ordered phase distribution along the grain boundaries due to texturing and phase separation.

Figure 16. Magnetic field patterns **(a)** when the ferrite particles are placed between the magnets; and **(b)** when ferrite plates are placed.

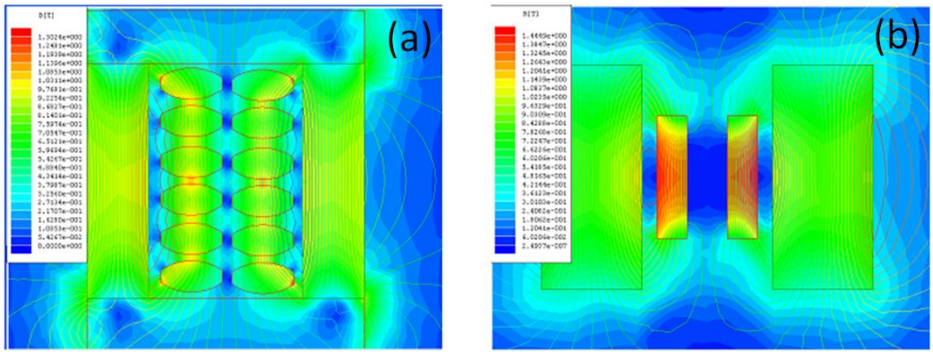

Figure 17. Transmission electron microscope images of PZT-NFO core-shell composite synthesized by high pressure compaction sintering: **(a)** Bright field **(b)** Dark field.

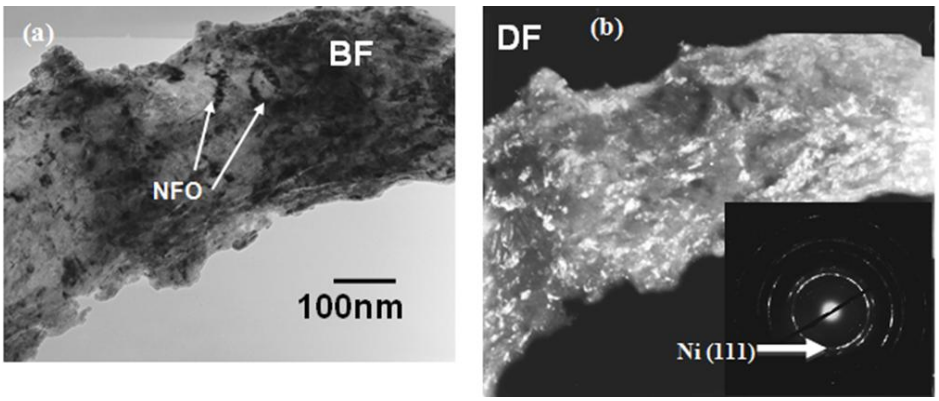

The lead-free 3-0 ME composites have been studied using three types of piezoelectric materials based on: (i) $K_{0.5}Na_{0.5}NbO_3$, (ii) $Na_{0.5}Bi_{0.5}TiO_3$, and (iii) $BaTiO_3$. $BaTiO_3$-$CoFeO_4$ (BTO-CFO) lead-free composites were reported by Boomgaard *et al*. in 1978 and were found to exhibit ME coefficient of 130 mV/cm·Oe [13]. After that, several studies have been conducted on lead-free ME composites but the magnitude of ME coefficient was found to be below 100 mV/cm·Oe in off-resonance conditions because of the poor piezoelectric properties of lead-free materials. Recently, lead-free 3-0 ME composites of $(1 - x)$ [0.948 $K_{0.5}Na_{0.5}NbO_3$–0.052 $LiSbO_3$] − x $Ni_{0.8}Zn_{0.2}Fe_2O_4$ (KNNLS-NZF) with island–matrix structure have been studied by Yang *et al*. [170]. Figure 18 shows that the ME voltage coefficient was found to maximize in the 0.7 KNNLS–0.3 NZF sintered at 1060 ℃ and the optimum DC bias representing the maximum ME voltage coefficient decreased with increase in mole fraction of NZF in the composites. From the result in Figure 18(a), it can be also seen that the island-matrix system is a promising structure to use wide range of magnetic values with high ME effect.

Figure 18. (a) ME coefficient and **(b)** H_{bias} for (1 − x) KNNLS–x NZF composites.

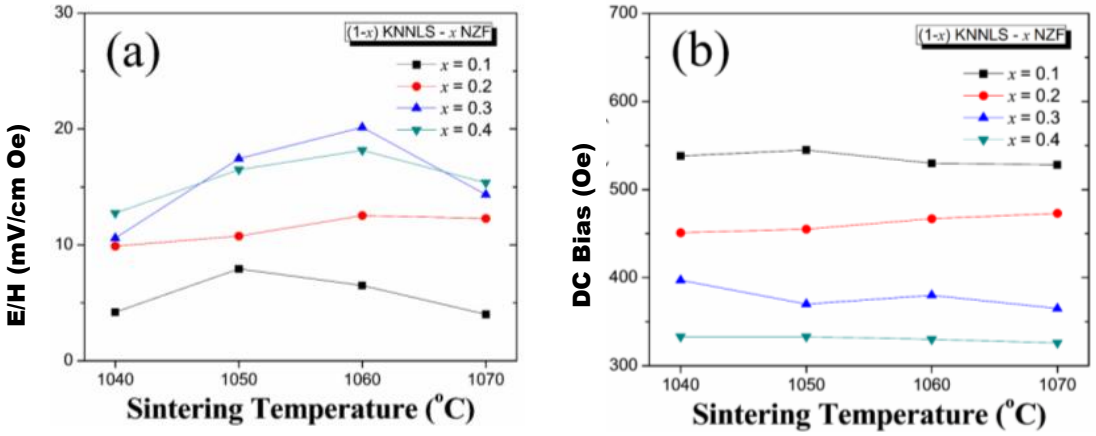

5.2. ME Effect in 2-2 Composites

A 2-2 connectivity refers to a bilayer consisting of piezoelectric and magnetostrictive phases [8]. The leakage problem due to high concentration of ferrite and low resistivity in the ferroelectric ceramic matrix can be eliminated through laminate structure as shown in Figure 19. However, high temperature co-firing process for the piezoelectric and ferrite ceramic layers is a big challenge due to difference in shrinkage rate, thermal expansion mismatch, and interdiffusion and/or chemical reactions between the two ceramic layers during the sintering process at high temperature. These composites also exhibit much larger anisotropy as compared to particulate composites.

Figure 19. Schematic diagram of ME trilayer composites with two-type configurations.

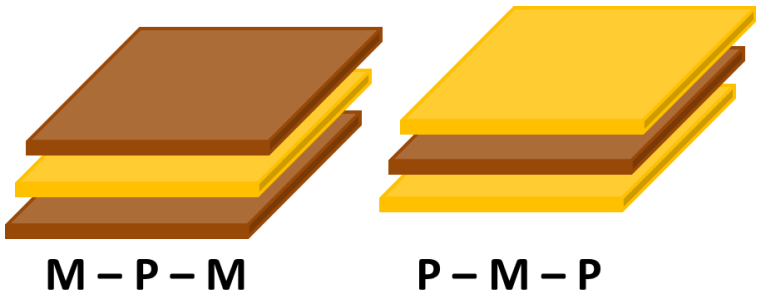

Figure 20 summarizes the magnitude of ME coefficient reported for 2-2 laminate composites in off-resonance conditions. In general, 2-2 laminate ME composites, three types of magnetostrictive mateirals have been used: (i) ferrite, (ii) Terfenol-D, and (iii) Metglas. Various ferrite oxides in Table 6 are available to co-sinter with piezoelectric matrix and were found to exhibit different magnetostrictions due to their varying magnetic properties [171]. Terfenol-D has the largest magnetostriction of 1400 × 10^{-6} with low permeability, while Metglas has extremely high relative permeability of >40,000 and thus is an quite attractive magnetostrictive material in low field ME sensors [172]. Detailed research has been performed by the authors exploring the 2-2 connectivity of the ME composites in the form of bilayers, trilayers and multilayers of piezoelectric and magnetostrictive materials. Islam *et al*. have synthesized PZT-NCZF bilayer and NCZF-PZT-NCZF

trilayer using co-firing technique. We found a high ME coefficient on the order of ~500 mV/cm Oe in trilayer structures [164]. Lead-free 2-2 laminate ME composites of $BaTiO_3$ (BT) / $(Ni_{0.8}Zn_{0.2})Fe_2O_4$ (NZFO) also were synthesized by co-firing and the magnitude of ME voltage coefficient reached saturation at DC bias of 1000 Oe with maximum magnitude of 152 mV/cm Oe [173]. Dong *et al*. have studied several multilayered ME configurations by using materials PZT, Terfenol D and Metglas and have reported quite high ME coefficients on the order of 10 V/cm Oe in resonance condition [30,32,33,38]. Among bulk multiferroic composites, the composites consisting of giant magnetostrictive alloy $Tb_{1-x}Dy_xFe_2$ (Terfenol-D) and piezoelectric $Pb(Zr,Ti)O_3$ (PZT), exhibiting high magneto and electromechanical energy densities respectively, are the most attractive due to their giant ME response [33,34,38,174,175]. Recent research by Park *et al*. reported the maximum ME coefficient of 5150 mV/cm·Oe in off-resonance condition by combining PZT-PMN, Metglas, and Terfenol-D [176].

Table 6. Magnetostrictions for ferrite oxides.

Material	$\lambda s(\times 10^{-6})$
$MnFe_2O_4$	−5
Fe_3O_4	40
$CoFe_2O_4$	−110
$MgFe_2O_4$	−6
$Li_{0.5}Fe_{2.5}O_4$	−8
$NiFe_2O_4$	−26
$CuFe_2O_4$	−9
YFe_5O_{12}	−2
$SmFe_5O_{12}$	3.3
$DyFe_5O_{12}$	1.46
$EuFe_5O_{12}$	9.48

Our study on texturing in 2-2 laminate composites shows that the cofired ME trilayer consisting of $(Ni_{0.6}Cu_{0.2}Zn_{0.2})Fe_2O_3$ (NCZF) and $0.85Pb(Zr_{0.52}Ti_{0.48})O_3$-$0.15Pb(Zn_{1/3}Nb_{2/3})O_3$ (PZT–PZN) with partial texturing was found to exhibit 67 % improvement in magnitude of ME coefficient than that of trilayer with random orientation [177]. The textured PZT-PZN composites with high tetragonality were found to possess 44% improvement in d_{33} and 44–50% enhancement in dielectric constant. Park *et al*. reported ME responses in 2-2 laminate composites consisting of $Pb(Zn_{1/3}Nb_{2/3})_x(Zr_{0.5}Ti_{0.5})_{1-x}O_3$ (PZNT) and Metglas [178]. These laminates were fabricated by stacking 20 layers of Metglas on one-side of PZNT plate for type I and both-side of PZNT plate for type II composites as shown in Figure 21. The ME voltage coefficients were found to be 62 mV/cm Oe at DC bias of 215 Oe for type I and 73 mV/cm Oe at DC bias of 570 Oe. Dimensionally gradient bimorph structure has been designed for wide operating range of frequency and H_{bias} [179]. The ME behavior was found to be dependent on both shape and dimension of laminates such that the bimorph laminates with asymmetric H shape were found to exhibit flat ME responses by merging different dimensional ME responses under wide ranges of H_{bias} = 60−215 Oe and f = 7−22 kHz, respectively. Our results have laid the foundation for design of the magnetic field sensors exhibiting wide frequency and DC bias operating range.

Figure 20. Magnetoelectric coefficient for 2-2 laminate composites in off-resonance conditions.

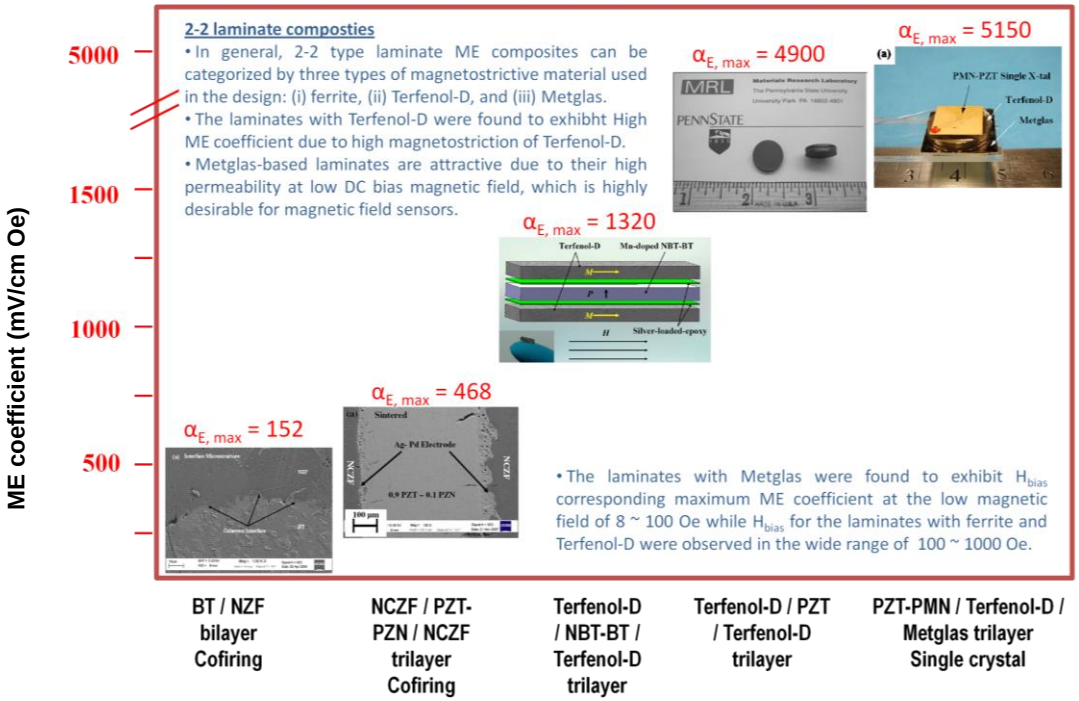

Figure 21. (a) Schematic diagram and **(b)** ME voltage coefficients for PZNT/Metglas bilayer and Metglas/PZNT/Metglas trilayer laminates.

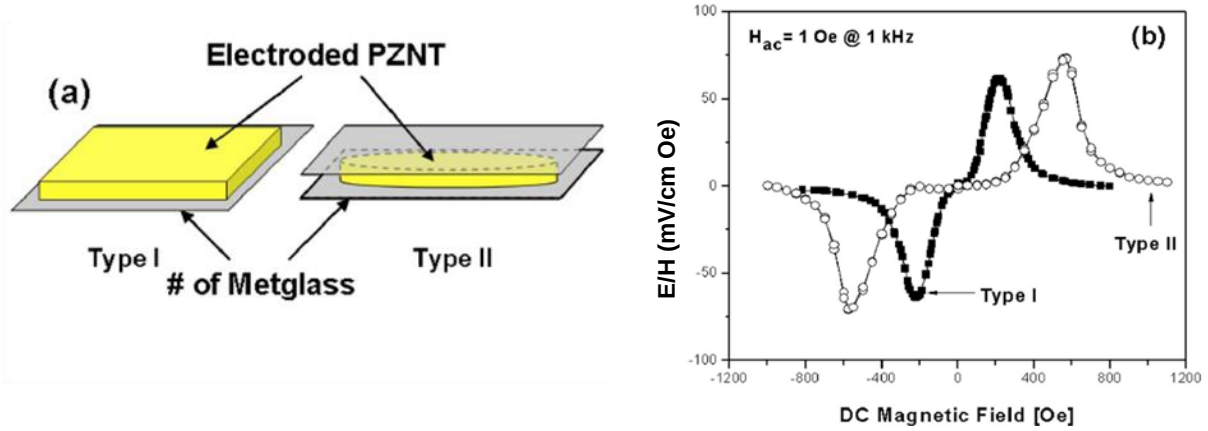

Recently, we have measured the ME voltage coefficients for 2-2 lead-free ME laminates given as Ni/NKNLS / Ni, Ni/NBTBT/Ni, and Metglas/NBTBT/Metglas. These lead-free ME laminates were fabricated by embedding piezoelectric layers between magnetostrictive layers of Ni plates or Metglas. The lead-free laminates with Ni in Figure 22 (a) and (b) were found to exhibit high ME coefficients of 300 and 80 mV/cm Oe at H_{bias} = 100 and 200 Oe, respectively. On the other hand, the laminates with Metglas shown in Figure 22 (c) show the maximum ME coefficient of 47 mV/cm Oe below 30 Oe due to the high permeability of Metglas.

Figure 22. ME voltage coefficients for 2-2 trilayer laminates of **(a)** Ni/NKNLS/Ni; **(b)** Ni/NBTBT/Ni; and **(c)** Metglas/NKNLS/Metglas.

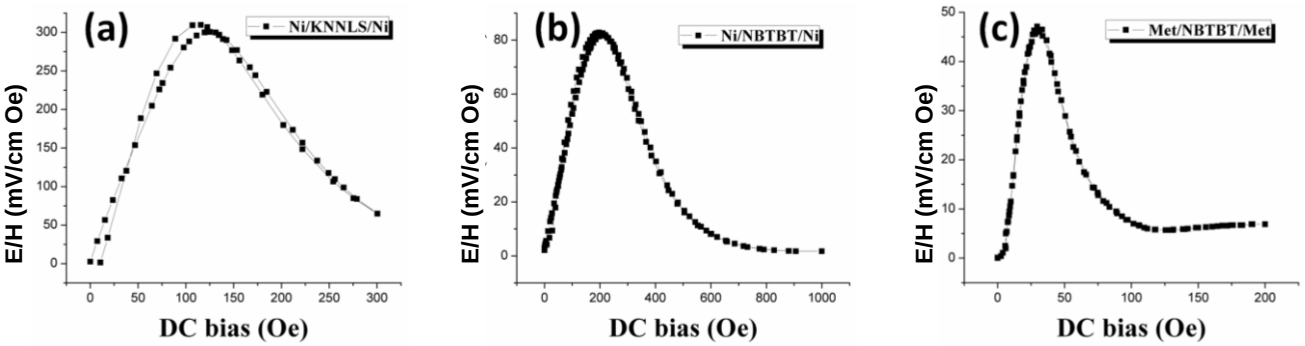

Figure 23. Longitudinal piezoelectric strain coefficient for (1 − x) KNNLS–x NZF composites as a function of atomic ratio of Fe/Nb. ME coefficient for (1 − x)KNNLS-xNZF / Ni / (1 − x)KNNLS-xNZF bending mode laminates: **(a)** x = 0.1; **(b)** x = 0.2; and **(c)** x = 0.3. Fe (white color) mapping images for (1 − x)KNNLS-xNZF composites: **(d)** x = 0.1; **(e)** x = 0.2; and **(f)** x = 0.3.

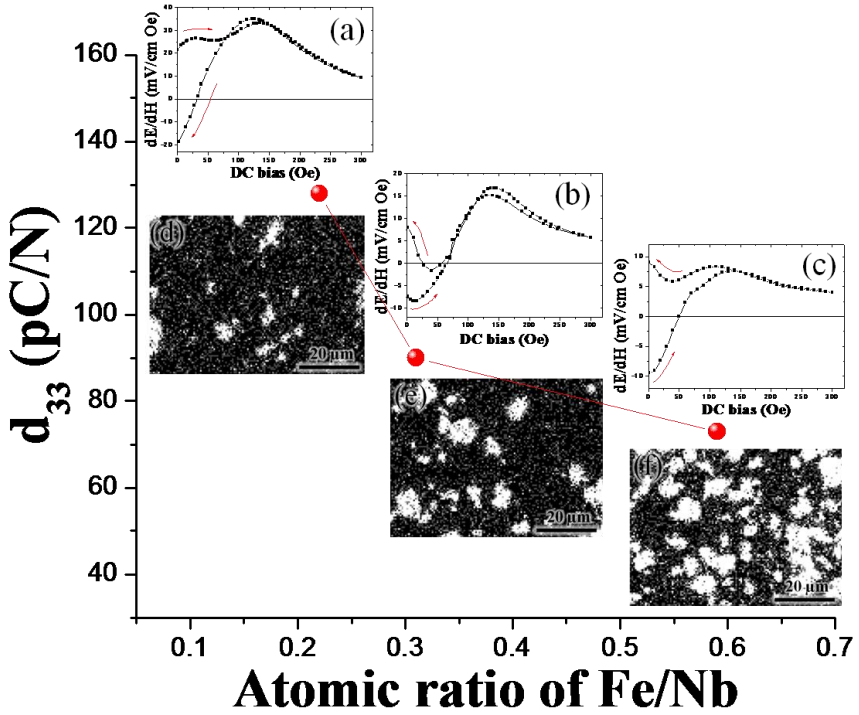

Effect of loss factors on dynamic ME response in 2-2 laminates has been reported by Cho *et al*. [180]. It was shown that the magnitude of ME sensitivity is dependent on intensive dielectric and piezoelectric loss in sub-resonance conditions but dominantly dependent on extensive mechanical loss in resonance conditions. We have designed ME laminate composites given as $Pb(Zr,Ti)O_3$-$Pb(Mg_{1/3}Nb_{2/3})O_3$ single crystal/Terfenol-D/Metglas for high sensitivity and found ME coefficient of 5 V/cm Oe at 1 kHz with DC magnetic sensitivity of 500 nT and 1 μT [176]. Recently, we have reported self-biased ME response, which is defined as remnant ME coefficient at zero *H* bias, in 2-2 ME laminate composites consisting of both one-phase piezoelectric and two-phase magnetostrictive layers with electric

connection for bending [181]. The ME hysteresis was found to be dependent on both magnetic interaction and bending effect, and various shapes of ME hysteresis could be obtained in off-resonance and resonance conditions. Recently, the material and structural effects on self-biased ME responses was realized by changing material composition, so that one could control the shape of ME hysteresis which can be promising for applications in low-field/high sensitive magnetic sensors and electrically, tuned memory devices as shown in Figure 23 [170].

5.3. ME Effect in 1-3 Composites

The ME coupling in 1-3 structure is considerably stronger than in 2-2 structure. In fact, ME effect in a 2-2 composite is determined by piezoelectric coefficient d_{31} and piezomagnetic coefficient $q_{11} + q_{12}$. For a 1-3 structure, the determining contribution arises from d_{33} and q_{11} since the stress components along the cylinders axis substantially exceed other components. Piezoelectric and piezomagnetic coefficients d_{33} and q_{11} are known to be about two times greater compared than d_{31} and $q_{11} + q_{12}$. In case of 3-0 composite, the observed decrease in ME coupling strength is caused by clamping the internal units of cubic model by neighboring ones. Clamping restricts the strains of composite and reduces the induced voltage across the piezoelectric phase. Figure 24 summarizes the magnitude of ME coefficient reported for 1-3 composites in off-resonance conditions.

Figure 24. Magnetoelectric coefficient for 1-3 composites in off-resonance conditions.

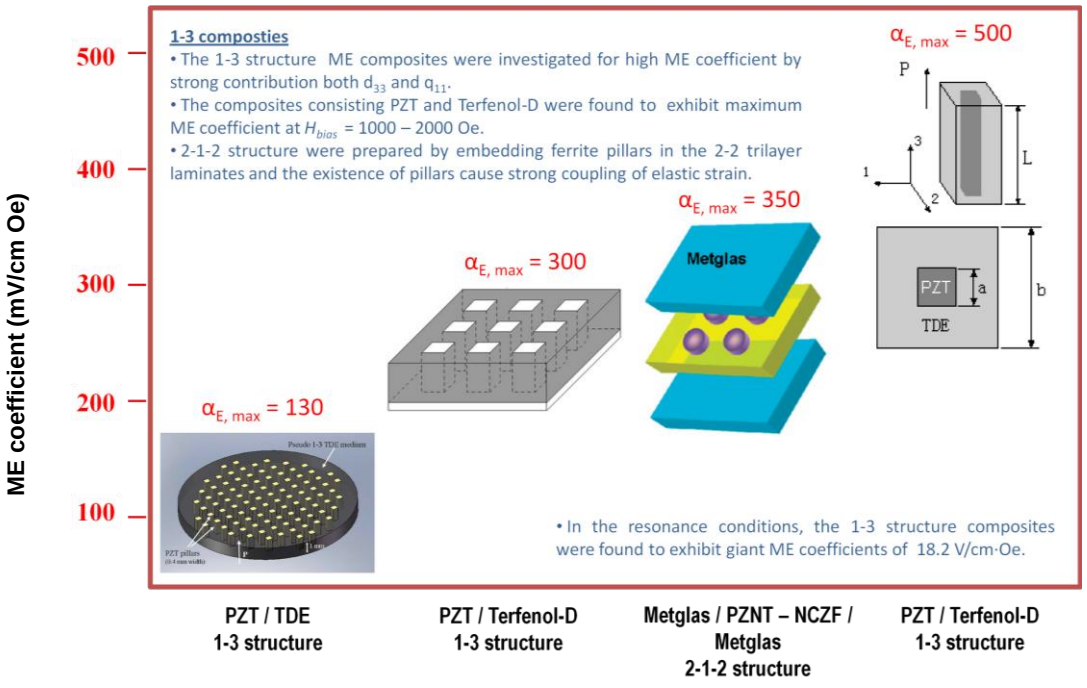

Several reports have been published in literature in order to achieve magnetic and magnetoelectric nanowires/nanocomposites exhibiting 1–3 mode. The development of the soft mold process allows for the preparation of fine scale 1–3 composites with PZT rods of different size, shape and spacing, which can be used as ultrasonic transducers for frequencies 55 MHz [182]. Ma *et al*. showed a single period of 1-3-type structured ME composite as shown in Figure 25. The experimental results demonstrated that the coupling interaction between the PZT rod and TDE medium can generate much larger ME

response. Especially at high frequency where the electromechanical resonance appears, the composite shows a giant ME effect. This single period 1-3-type composite presents a size-dependent ME response, Figure 24 indicates that micro/nano ME pillars with large ME response can be obtained and promises future micro-ME devices. Lam *et al*. reported frequency response of 1-3 ME composites consisting of $Pb(Zr,Ti)O_3$ (PZT) rods embedded in a matrix of Terfenol-D/epoxy (TDE) [183]. The composites were found to exhibit maximum ME coefficient of 130 mV/cm Oe at 1 kHz and the resonance shifts to lower frequency with increase in bias field. Also, the pseudo 1-3 ME composite consisting of PZT rod array and Terfenol-D/epoxy matrix were reported by Shi *et al*. [184] and the magnetoelectric coefficients were found to be 300 mV/cm Oe at off-resonance frequency and 4500 mV/cm Oe at resonant frequency.

Figure 25. Frequency dependence of the ME coefficients for the small ME composite rod with a/b = 0.25 and L/a = 1 mm.

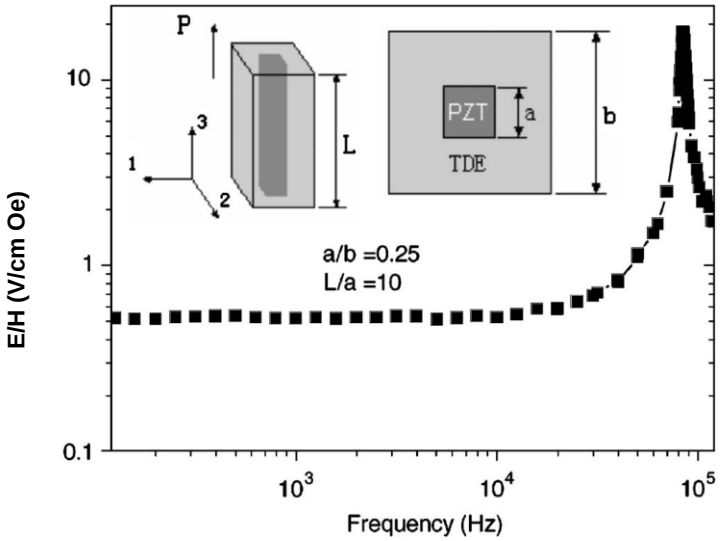

We consider a structure consisting of piezoelectric and magnetostrictive coaxial cylinders. Both cylinders are assumed to be ideally bonded together. Such a system is an example of 1-3 composite. For the sake of simplicity, we consider a poled state in both the piezoelectric and magnetostrictive phases with the poling directed along the axis of cylinders (*z* axis). The applied ac magnetic field is also assumed to be directed along *z* axis. As a result, the induced electric field also has the same direction. How to solve the problem of ME coupling in a 3-1 or 1-3 magnetostrictive-piezoelectric nanocomposite on a substrate is described in our previous work [185]. To adapt that model to the structure to be considered, we ignore the substrate clamping and lattice mismatch effect. Taking into account the axial symmetry of structure, the elastostatic equation is written in cylindrical coordinates system:

$$\frac{\partial T_{rr}}{\partial r} + \frac{1}{r}(T_{rr} - T_{\theta\theta}) = 0. \tag{85}$$

Transferring Equations (79) and (80) to cylindrical coordinates and expressing the stress tensor component in terms of strain tensor component, one can substitute the found expressions into

Equation (85). As a result, the following equation can be obtained for the radial displacement u_r that defines strain components $S_{rr}=\partial u_r/\partial r$ and $S_{\theta\theta}=u_r/r$ for both phases:

$$\frac{\partial^2 u_r}{\partial r^2}+\frac{1}{r}\frac{\partial u_r}{\partial r}-\frac{u_r}{r^2}=0. \tag{86}$$

The boundary conditions in this case have the form:

$$\begin{gathered} {}^{p}u_r = 0 \text{ at } r=0, \\ {}^{p}u_r = {}^{m}u_r \text{ and } {}^{p}T_r = {}^{m}T_r \text{ at } r = {}^{p}R \\ {}^{m}T_r = 0 \text{ at } r = {}^{m}R \\ {}^{p}S_{zz} = {}^{m}S_{zz}, \\ \int_0^{{}^{p}R} {}^{p}T_{zz} r dr = -\int_{{}^{p}R}^{{}^{m}R} {}^{m}T_{zz} r dr \end{gathered} \tag{87}$$

where ${}^{p}R$ and ${}^{m}R$ are radii of piezoelectric and piezomagnetic phases. Equations (79), (86), (87) and open circuit condition $D_3 = 0$ constitute a closed system and can be numerically solved for ME voltage coefficient $\alpha_{E,33}$. Estimates are shown in Figure 26 for NZFO-PZT, NZFO-MBT-BT, NZFO-Mn:MBT-BT, and NZFO-NKN-BT structures with sample thickness of 1 mm. It should be noted that the PZT volume fraction dependence of ME voltage coefficient for a 3–1 composite is similar to that of 1-3 composite in Figure 24.

Figure 26. Piezoelectric volume fraction dependence of ME voltage coefficient for 1–3 composites of NZFO-PZT, NZFO-NBTBT, NZFO-Mn:NBTBT, and NZFO-NKNBT.

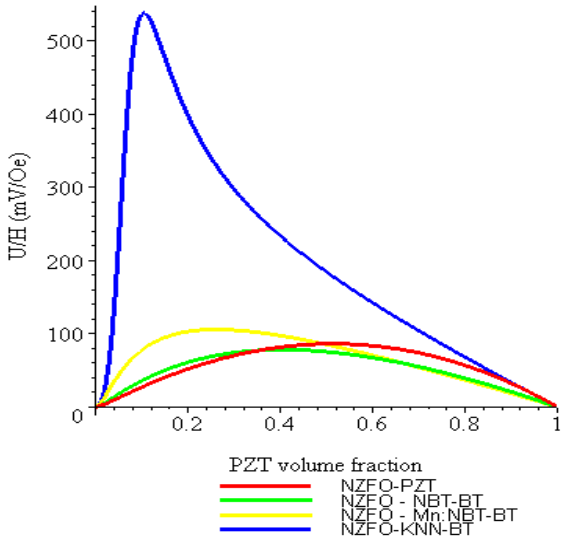

In our study on 2-1-2 ME laminate composites having configuration of Metglas/0.2Pb($Zn_{1/3}Nb_{2/3}$)O_3-0.8Pb($Zr_{0.5}Ti_{0.5}$)O_3 (PZNT)/Metglas with ferrite pillars embedded in the PZNT phase [186]. The piezoelectric layer with composition PZNT consisted of co-fired $(Ni_{0.6}Cu_{0.2}Zn_{0.2})Fe_2O_3$ (NCZF) pillars as shown in Figure 27 (a). The 2-1-2 composite was found to exhibit the ME coefficient of

352 mV/cm Oe which is 15% higher magnitude than that for 2-2 laminate composites by effective coupling in the 2-1-2 structure as shown in Figure 27 (b) and (c). The result shows the existence of NCNF pillars in 2-1-2 laminates causes strong coupling of elastic strain.

Figure 27. (a) Schematic diagrams of unimorph and bimorph configurations; **(b)** ME coefficient of 3-1 composite depending on the laminations: 3-1/Metglas and Metglas/3-1/Metglas; **(c)** ME coefficient of typical 2-2 composites based on PZNT and Metglas: unimorph and bimorph configurations.

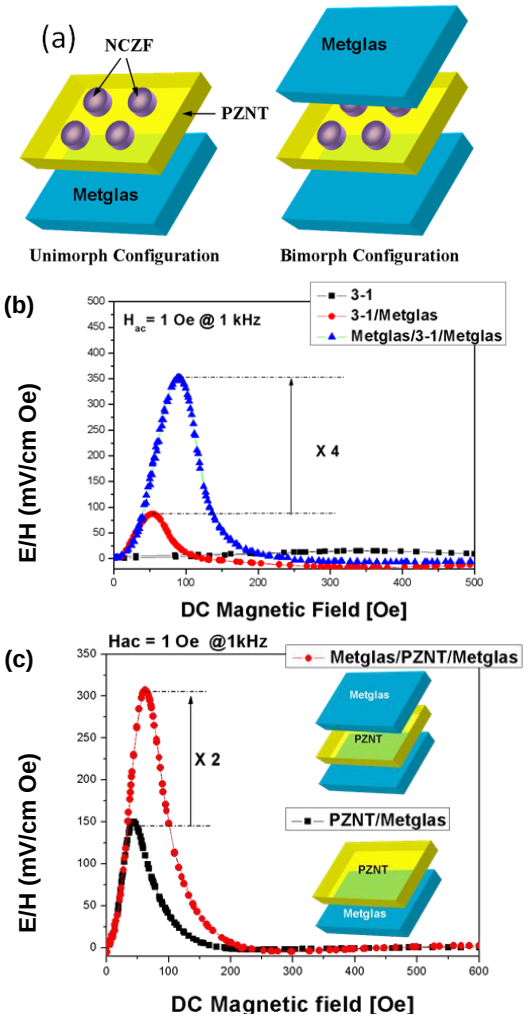

6. Conclusions

In this manuscript, we report the ME characterization of composites based on magnetostrictive NZFO or Ni and piezoelectric PZT and lead-free ferroelectrics. The piezoelectric volume fraction dependence of ME coefficients is calculated using the physical parameters of composite components. In order to overcome the problem of toxicity of Pb, we conducted experiments with Pb-free piezoelectric compositions illustrating their importance as an environment friendly alternative. To estimate the piezoelectric parameters of lead-free materials, we used the thermodynamic LGD approach and generalized lattice model of ferroelectric solid solutions. It has been shown that

composites based on lead-free ferroelectrics can exhibit the ME couling that is at least not weaker compared to leaded materials.

Acknowledgments

The authors gratefully acknowledge the financial support from National Science Foundation and Office of Basic Energy Science, Department of Energy, Russian Foundation for Basic Research (project No. 08-02-91359-SNF_a), Program of Russian Ministry of Education and Science "Scientific and pedagogical personnel of innovative Russia" on 2009–2013, Project of Russian Ministry of Education and Science-Section 2.1.2-Fundamental researches in technical sciences (Project No.11324), and Department of Chemistry and Material Science of Russian Academy of Sciences.

References

1. Van Suchetelen, J. Product Properties: A new application of composite materials. *Philips Res. Rep*. **1972**, *27*, 28-37.
2. Smolenskii, G.; Ioffe, V.A. Communication No. 71. *Colloque Int. du Magnetisme Grenoble* **1958**, 71-75.
3. Astrov, D.N.; Aleshin, B.I.; Zorin R.V.; Drobyshev, L.A. On spontaneous magnetoelectric effect. *Sov. Phys. JETP* **1968**, *28*, 1123-1127.
4. Fiebig, M. Revival of the magnetoelectric effect. *J. Phys.-D-Appl. Phys.* **2005**, *38*, R123-R152.
5. Bichurin, M.I.; Petrov, V.M.; Petrov, R.V.; Kapralov, G.N.; Kiliba, Y.V.; Bukashev, F.I.; Smirnov, A.Y.; Tatarenko, A.S. Magnetoelectric microwave devices. *Ferroelectrics* **2002**, *280*, 377-384.
6. Nan, C.W.; Bichurin, M.I.; Dong, S.X.; Viehland, D.; Srinivasan, G. Multiferroic magnetoelectic composites: Historical perspective, status, and future directions. *J. Appl. Phys.* **2008**, *103*, 031101:1-031101:35.
7. Hornreich, R.M. The magnetoelectric effect: Some likely candidates. *Solid State Commun.* **1969**, *7*, 1081-1085.
8. Bichurin, M.I.; Petrov, V.M.; Srinivasan, G. Theory of low-frequency magnetoelectric coupling in magnetostrictive-piezoelectric bilayers. *Phys. Rev. B* **2003**, *68*, 054402:1-054402:13.
9. Fischer, E.; Gorodetsky, G.; Hornreich, R.M. A new family of magnetoelectric materials: $A_2M_4O_9$ (A = Ta, Nb; M = Mn, Co). *Solid State Commun.* **1972**, *10*, 1127-1132.
10. Suryanarayana, S.V. Magnetoelectric interaction phenomena in materials. *Bull. Mater. Sci.* **1994**, *17*, 1259-1270.
11. Srinivas, A.; Kim, D.W.; Hong, K.S.; Suryanarayana, S.V. Study of magnetic and magnetoelectric measurements in bismuth iron titanate ceramic—$Bi_8Fe_4Ti_3O_{24}$. *Mater. Res. Bull.* **2004**, *39*, 55-61.
12. Van den Boomgaard, J.; Terrell, D.R.; Born, R.A.; Giller, H.F. An *in situ* grown eutectic magnetoelectric composite material. *Mater. Sci.* **1974**, *9*, 1705-1709.
13. Van den Boomgaard, J.; Born, R.A. Sintered magnetoelectric composite-material $BaTiO_3$-Ni(Co,Mn)Fe_2O_4. *J. Mater. Sci.* **1978**, *13*, 1538-1548.

14. Dai, Y.R.; Bao, P.; Zhu, J.S.; Wan, J.G.; Shen, H.M.; Liu, J.M. Internal friction study on CuFe2O4/PbZr0.53Ti0.47O3 composites. *J. Appl. Phys.* **2004**, *96*, 5687-5690.
15. Ruette, B.; Zvyagin, S.; Pyatakov, A.P.; Bush, A.; Li, J.F.; Belotelov, V.I.; Zvezdin, A.K.; Viehland, D. Magnetic-field-induced phase transition in $BiFeO_3$ observed by high-field electron spin resonance: Cycloidal to homogeneous spin order. *Phys. Rev. B* **2004**, *69*, 064114:1-064114:7.
16. Kadomtseva, A.M.; Zvezdin, A.K.; Popov, Y.F.; Pyatakov, A.P.; Vorobev, G.P. Space-time parity violation and magnetoelectric interactions in antiferromagnets. *JETP Lett-Engl. Tr.* **2004**, *79*, 571-581.
17. Wang, J.; Neaton, J.B.; Zheng, H.; Nagarajan, V.; Ogale, S.B.; Liu, B.; Viehland, D.; Vaithyanathan, V.; Schlom, D.G.; Waghmare, U.V.; Spaldin, N.A.; Rabe, K.M.; Wuttig, M.; Ramesh, R. Epitaxial BiFeO3 multiferroic thin film heterostructures. *Science* **2003**, *299*, 1719-1722.
18. Kimura, T.; Goto, T.; Shintani, H.; Ishizaka, K.; Arima, T.; Tokura, Y. Magnetic control of ferroelectric polarization. *Nature* **2003**, *426*, 55-58.
19. Fiebig, M.; Lottermoser, T.; Frohlich, D.; Goltsev, A.V.; Pisarev, R.V. Observation of coupled magnetic and electric domains. *Nature* **2002**, *419*, 818-820.
20. Ederer, C.; Spaldin, N.A. Magnetoelectrics—A new route to magnetic ferroelectrics. *Nat. Mater.* **2004**, *3*, 849-851.
21. Hur, N.; Park, S.; Sharma, P.A.; Ahn, J.S.; Guha, S.; Cheong, S.W. Electric polarization reversal and memory in a multiferroic material induced by magnetic fields. *Nature* **2004**, *429*, 392-395.
22. Lottermoser, T.; Lonkai, T.; Amann, U.; Hohlwein, D.; Ihringer, J.; Fiebig, M. Magnetic phase control by an electric field. *Nature* **2004**, *430*, 541-544.
23. Van Aken, B.B.; Palstra, T.T.; Filippetti, A.; Spaldin, N.A. The origin of ferroelectricity in magnetoelectric $YMnO_3$. *Nat. Mate.* **2004**, *3*, 164-170.
24. Srinivasan, G.; DeVreugd, C.P.; Flattery, C.S.; Laletsin, V.M.; Paddubnaya, N. Magnetoelectric interactions in hot-pressed nickel zinc ferrite and lead zirconante titanate composites. *Appl. Phys. Lett.* **2004**, *85*, 2550-2552.
25. Ryu, J.; Priya, S.; Uchino, K.; Kim, H.E. Magnetoelectric effect in composites of magnetostrictive and piezoelectric materials. *J. Electroceram.* **2002**, *8*, 107-119.
26. Srinivasan, G.; Rasmussen, E.T.; Hayes, R. Magnetoelectric effects in ferrite-lead zirconate titanate layered composites: The influence of zinc substitution in ferrites. *Phys. Rev. B* **2003**, *67*, 014418:1-014418:10.
27. Srinivasan, G.; Rasmussen, E.T.; Levin, B.J.; Hayes, R. Magnetoelectric effects in bilayers and multilayers of magnetostrictive and piezoelectric perovskite oxides. *Phys. Rev. B* **2002**, *65*, 134402:1-134402:7.
28. Ryu, J. Carazo, A.V.; Uchino, K.; Kim, H.E. Magnetoelectric properties in piezoelectric and magnetostrictive laminate composites *Jpn. J. Appl. Phys.* **2001**, *40*, 4948-4951.
29. Laletin, V.M.; Padubnaya, N.; Srinivasan, G.; Devreugd, C.P. Frequency dependence of magnetoelectric interactions in layered structures of ferromagnetic alloys and piezoelectric oxides. *Appl. Phys. A-Mat. Sci. Process.* **2004**, *78*, 33-36.
30. Dong, S.X.; Zhai, J.Y.; Li, J.F.; Viehland, D. Small DC magnetic field response of magnetoelectric laminate composites. *Appl. Phys. Lett.* **2006**, *88*, 082907:1-082907:2.

31. Dong, S.X.; Li, J.F.; Viehland, D. Longitudinal and transverse magnetoelectric voltage coefficients of magnetostrictive/piezoelectric laminate composite: Theory. *IEEE T. Ultrason. Ferroelectr.* **2003**, *50*, 1253-1261.
32. Dong, S.X.; Li, J.F.; Viehland, D. Circumferentially magnetized and circumferentially polarized magnetostrictive/piezoelectric laminated rings. *J. Appl. Phys.* **2004**, *96*, 3382-3387.
33. Dong, S.X.; Cheng, J.R.; Li, J.F.; Viehland, D. Enhanced magnetoelectric effects in laminate composites of Terfenol-D/Pb(Zr,Ti)O-3 under resonant drive. *Appl. Phys. Lett.* **2003**, *83*, 4812-4814.
34. Dong, S.X.; Li, J.F.; Viehland, D. A longitudinal-longitudinal mode TERFENOL-D/Pb $(Mg_{1/3}Nb_{2/3})O_3$3-$PbTiO_3$ laminate composite. *Appl. Phys. Lett.* **2004**, *85*, 5305-5306.
35. Dong, S.X.; Zhai, J.Y.; Xing, Z.P.; Li, J.F.; Viehland, D. Extremely low frequency response of magnetoelectric multilayer composites. *Appl. Phys. Lett.* **2005**, *86*, 102901:1-102901:3.
36. Zhai, J.Y.; Xing, Z.P.; Dong, S.X.; Li, J.F.; Viehland, D. Detection of pico-Tesla magnetic fields using magneto-electric sensors at room temperature. *Appl. Phys. Lett.* **2006**, *88*, 062510:1-062510:3.
37. Dong, S.X.; Li, J.F.; Viehland, D. Vortex magnetic field sensor based on ring-type magnetoelectric laminate. *Appl. Phys. Lett.* **2004**, *85*, 2307-2309.
38. Dong, S.X.; Li, J.F.; Viehland, D.; Cheng, J.; Cross, L.E. A strong magnetoelectric voltage gain effect in magnetostrictive-piezoelectric composite. *Appl. Phys. Lett.* **2004**, *85*, 3534-3536.
39. Dong, S.X.; Li, J.F.; Viehland, D. Longitudinal and transverse magnetoelectric voltage coefficients of magnetostrictive/piezoelectric laminate composite: Experiments. *IEEE T. Ultrason. Ferroelectr.* **2004**, *51*, 794-799.
40. Dong, S.X.; Zhai, J.Y.; Bai, F.M.; Li, J.F.; Viehland, D.; Lograsso, T.A. Magnetostrictive and magnetoelectric behavior of Fe-20 at. % Ga/Pb(Zr,Ti)O-3 laminates. *J. Appl. Phys.* **2005**, *97*, 103902:1-103902:6.
41. Dong, S.X.; Zhai, J.Y.; Wang, N.G.; Bai, F.M.; Li, J.F.; Viehland, D.; Lograsso, T.A. Fe-Ga/$Pb(Mg_{1/3}Nb_{2/3})O_3$-$PbTiO_3$ magnetoelectric laminate composites. *Appl. Phys. Lett.* **2005**, *87*, 222504:1-222504:3.
42. Jia, Y.M.; Or, S.W.; Chan, H.L.; Zhao, X.Y.; Luo, H.S. Converse magnetoelectric effect in laminated composites of PMN-PT single crystal and Terfenol-D alloy. *Appl. Phys. Lett.* **2006**, *88*, 242902:1-242902:3.
43. Wan, J.G.; Liu, J.M.; Wang, G.H.; Nan, C.W. Electric-field-induced magnetization in $Pb(Zr,Ti)O_3$/Terfenol-D composite structures. *Appl. Phys. Lett.* **2006**, *88*, 182502:1-182502:3.
44. Ryu, J.; Priya, S.; Uchino, K.; Viehland, D.; Kim, H. High magnetoelectric properties in 0.68$Pb(Mg_{1/3}Nb_{2/3})O_3$-0.32$PbTiO_3$ single crystal and Terfenol-D laminate composite. *J. Korean Ceram. Soc.* **2002**, *39*, 813-817.
45. Babu, S.N.; Bhimasankaram T.; Suryanarayana, S.V. Magnetoelectric effect in metal-PZT laminates. *Bull. Mater. Sci.* **2005**, *28*, 419-422.
46. Laletin, V.M.; Paddubnaya, N.; Srinivasan, G.; De Vreugd, C.P.; Bichurin, M.I.; Petrov, V.M.; Filippov, D.A. Frequency and field dependence of magnetoelectric interactions in layered ferromagnetic transition metal-piezoelectric lead zirconate titanate. *Appl. Phys. Lett.* **2005**, *87*, 222507:1-222507:3.

47. Nan, C.W.; Liu, L.; Cai, N.; Zhai, J.Y.; Ye, Y.; Lin, Y.H.; Dong, L.J.; Xiong, C.X. A three-phase magnetoelectric composite of piezoelectric ceramics, rare-earth iron alloys, and polymer. *Appl. Phys. Lett.* **2002**, *81*, 3831-3833.
48. Shi, Z.; Nan, C.W.; Liu, J.M.; Filippov, D.A.; Bichurin, M.I. Influence of mechanical boundary conditions and microstructural features on magnetoelectric behavior in a three-phase multiferroic particulate composite. *Phys. Rev. B* **2004**, *70*, 134417:1-134417:6.
49. Dong, S.X.; Zhai, J.Y.; Bai, F.M.; Li, J.F.; Viehland, D. Push-pull mode magnetostrictive/ piezoelectric laminate composite with an enhanced magnetoelectric voltage coefficient. *Appl. Phys. Lett.* **2005**, *87*, 062502:1-062502:3.
50. Dong, S.X.; Li, J.F.; Viehland, D. Giant magneto-electric effect in laminate composites. *IEEE T. Ultrason. Ferroelectr.* **2003**, *50*, 1236-1239.
51. Dong, S.X.; Li, J.F.; Viehland, D. Magnetoelectric coupling, efficiency, and voltage gain effect in piezoelectric-piezomagnetic laminate composites. *J. Mater. Sci.* **2006**, *41*, 97-106.
52. Cai, N.; Zhai, J.Y.; Nan, C.W.; Lin Y.; Shi, Z. Dielectric, ferroelectric, magnetic, and magnetoelectric properties of multiferroic laminated composites. *Phys. Rev. B* **2003**, *68*, 224103:1-224103:7.
53. Corral-Flores, V.; Bueno-Baques, D.; Carrillo-Flores D.; Matutes-Aquino, J.A. Enhanced magnetoelectric effect in core-shell particulate composites. *J. Appl. Phys.* **2006**, *99*, 08J503:1-08J503:3.
54. Mazumder S.; Bhattacharyya, G.S. Synthesis and characterization of *in situ* grown magnetoelectric composites in the BaO-TiO-FeO-CoO system. *Ceram. Int.* **2004**, *30*, 389-392.
55. Lupeiko, T.G.; Lopatin, S.S.; Lisnevskaya I.V.; Zvyagintsev, B.I. Magnetoelectric composite-materials based on lead-zirconate-titanate and nickel ferrite. *Inorg. Mater-Engl. Tr.* **1994**, *30*, 1353-1356.
56. Patankar, K.K.; Patil, S.A.; Sivakumar, K.V.; Mahajan, R.P.; Kolekar, Y.D.; Kothale, M.B. AC conductivity and magnetoelectric effect in $CuFe_{1.6}Cr_{0.4}O_4$-$BaTiO_3$ composite ceramics. *Mater. Chem. Phys.* **2000**, *65*, 97-102.
57. Yang, P.; Zhao, K.; Yin, Y.; Wan, J.G.; Zhu, J.S. Magnetoelectric effect in magnetostrictive/piezoelectric laminate composite Terfenol-D/LiNbO3 [(zxtw)-129 ?30 ?]. *Appl. Phys. Lett.* **2006**, *88*, 172903:1-172903:3.
58. Jia, Y.M.; Zhao, X.Y.; Luo, H.S.; Or, S.W.; Chan, H.L. Magnetoelectric effect in laminate composite of magnets/0.7$Pb(Mg_{1/3}Nb_{2/3})O_3$-0.3$PbTiO_3$ single crystal. *Appl. Phys. Lett.* **2006**, *88*, 142504:1-142504:3.
59. Zhao, K.; Chen, K.; Dai, Y.R.; Wan, J.G.; Zhu, J.S. Effect of martensitic transformation on magnetoelectric properties of Ni2MnGa/PbZr0.52Ti0.48O3 composite. *Appl. Phys. Lett.* **2005**, *87*, 162901:1-162901:3.
60. Shi, Z.; Nan, C.W.; Zhang, J.; Cai, N.; Li, J.F. Magnetoelectric effect of $Pb(Zr,Ti)O_3$ rod arrays in a $(Tb,Dy)Fe_2$ /epoxy medium. *Appl. Phys. Lett.* **2005**, *87*, 012503:1-012503:3.
61. Bichurin, M.I.; Filippov, D.A.; Petrov, V.M.; Laletin, V.M.; Paddubnaya, N.; Srinivasan, G. Resonance magnetoelectric effects in layered magnetostrictive-piezoelectric composites. *Phys. Rev. B* **2003**, *68*, 132408:1-132408:4.

62. Guo, Y.P.; Kakimoto, K.; Ohsato, H. Phase transitional behavior and piezoelectric properties of (Na0.5K0.5)NbO3-LiNbO3 ceramics. *Appl. Phys. Lett.* **2004**, *85*, 4121-4123.
63. Guo, Y.P.; Kakimoto, K.; Ohsato, H. (Na0.5K0.5)NbO3-LiTaO3 lead-free piezoelectric ceramics *Mater. Lett.* **2005**, *59*, 241-244.
64. Zang, G.Z.; Wang, J.F.; Chen, H.C.; Su, W.B.; Wang, C.M.; Qi, P.; Ming, B.Q.; Du, J.; Zheng, L.M. Perovskite $(Na_{0.5}K_{0.5})_{1-x}(LiSb)_xNb_{1-x}$ O_3 lead-free piezoceramics. *Appl. Phys. Lett.* **2006**, *88*, 212908:1-212908:3.
65. Ming, B.Q.; Wang, J.F.; Qi, P.; Zang, G.Z. Piezoelectric properties of (Li, Sb, Ta) modified (Na,K)NbO_3 lead-free ceramics. *J. Appl. Phys.* **2007**, *101*, 054103:1-054103:4.
66. Ahn, C.W.; Park, H.Y.; Nahm, S.; Uchino, K.; Lee H.G.; Lee, H.J. Structural variation and piezoelectric properties of 0.95(Na0.5K0.5)NbO_3-0.05$BaTiO_3$ ceramics. *Sensor. Actuator. A Phys.* **2007**, *136*, 255-260.
67. Wang, R.P.; Xie, R.J.; Hanada, K.; Matsusaki, K.; Bando, H.; Itoh, M. Phase diagram and enhanced piezoelectricity in the strontium titanate doped potassium-sodium niobate solid solution. *Phys. Status. Solidi. A Appl. Mat.* **2005**, *202*, R57-R59.
68. Wang, R.P.; Xie, R.J.; Hanada, K.; Matsusaki, K.; Bando, H.; Sekiya, T.; Itoh, M. Phase diagram of the $(Na_{0.5}K_{0.5})NbO_3$-$ATiO_3$ solid solution. *Ferroelectrics* **2006**, *336*, 39-46.
69. Park, H.Y.; Cho, K.H.; Paik, D.S.; Nahm, S.; Lee, H.G.; Kim, D.H. Microstructure and piezoelectric properties of lead-free (1-x)$(Na_{0.5}K_{0.5})NbO_3$-x$CaTiO_3$ ceramics. *J. Appl. Phys.* **2007**, *102*, 124101:1-124101:5.
70. Smolenskii, G.A.; Isupov, V.A.; Agranovskaya, A.I.; Krainik, N.N. New ferroelectrics complex composition—IV. *Sov. Phys. Solid State* **1961**, *2*, 2651-2654.
71. Jones, G.O.; Thomas, P.A. Investigation of the structure and phase transitions in the novel A-site substituted distorted perovskite compound $Na_{0.5}Bi_{0.5}TiO_3$. *Acta. Crystallogr. B Struct. Sci.* **2002**, *58*, 168-178.
72. Suchainicz, J.; Roleder, K.; Kania, A.; Handerek, J. Electrostrictive Strain and Pyroeffect in the Region of Phase Coexistence in $Na_{0.5}Bi_{0.5}TiO_3$. *Ferroelectrics* **1998**, *77*, 107-110.
73. Roleder, K.; Suchainicz, J.; Kania, A. Time-dependence of electric permittivity in $Na_{0.5}Bi_{0.5}TiO_3$ single-crystals. *Ferroelectrics* **1989**, *89*, 1-5.
74. Suchainicz, J. Investigations of the Phase Transitions in $Na_{0.5}Bi_{0.5}TiO_3$. *Ferroelectrics* **1995**, *172*, 455-458.
75. Tu, C.S.; Huang, S.H.; Ku, C.S.; Lee, H.Y.; Chien, R.R.; Schmidt, V.H.; Luo, H. Phase coexistence and Mn-doping effect in lead-free ferroelectric $(Na_{1/2}Bi_{1/2})TiO_3$ crystals. *Appl. Phys. Lett.* **2010**, *96*, 062903:1-062903:3.
76. Takenaka, T.; Maruyama, K.; Sakata, K. $(Bi_{1/2}Na_{1/2})TiO_3$-$BaTiO_3$ system for lead-free piezoelectric ceramics. *Jpn. J. Appl. Phys*. **1991**, *30*, 2236-2239.
77. Kuharuangrong, S.; Schulze, W. Compositional modifications of 10-percent-Pb-doped $Bi_{0.5}Na_{0.5}TiO_3$ for high-temperature dielectrics. *J. Amer. Ceram. Soc.* **1995**, *78*, 2274-2278.
78. Elkechai, O.; Manier, M.; Mercurio, J.P. $Na_{0.5}Bi_{0.5}TiO_3$-$K_{0.5}Bi_{0.5}TiO_3$ (NBT-KBT) system: A structural and electrical study. *Phys. Status. Solidi. A-Appl. Res.* **1996**, *157*, 499-506.
79. Takenaka, T.; Sakata, K.; Toda, K. Piezoelectric properties of $(Bi_{1/2}Na_{1/2})TiO_3$-based ceramics. *Ferroelectrics* **1990**, *106*, 375-380.

80. Marchet, P.; Boucher, E. Dorcet, V.; Mercurio, J.P. Dielectric properties of some low-lead or lead-free perovskite-derived materials: $Na_{0.5}Bi_{0.5}TiO_3$-$PbZrO_3$, $Na_{0.5}Bi_{0.5}TiO_3$-$BiScO_3$ and $Na_{0.5}Bi_{0.5}TiO_3$-$BiFeO_3$ ceramics. *J. Eur. Ceram. Soc.* **2006**, *26*, 3037-3041.
81. Nagata, H.; Takenaka, T. Lead-free piezoelectric ceramics of $(Bi_{1/2}Na_{1/2})TiO_3$-1/2(Bi_2O_3 center dot Sc_2O_3) system. *Jpn. J. Appl. Phys. Pt. 1* **1997**, *36*, 6055-6057.
82. Nagata, H.; Koizumi, N.; Kuroda, N.; Igarashi, I.; Takenaka, T. Lead-free piezoelectric ceramics of $(Bi_{1/2}Na_{1/2})TiO_3$-$BaTiO_3$-$BiFeO_3$ system. *Ferroelectrics* **1999**, *229*, 273-278.
83. Li, Y.M.; Chen, W.; Zhou, J.; Xu, Q.; Sun, H.; Xu, R.X. Dielectric and piezoelecrtic properties of lead-free $(Na_{0.5}Bi_{0.5})TiO_3$-$NaNbO_3$ ceramics. *Mater. Sci. Eng. B-Solid State M.* **2004**, *112*, 5-9.
84. Sung, Y.S.; Kim, J.M.; Cho, J.H.; Song, T.K.; Kim, M.H.; Chong, H.H.; Park, T.G.; Do, D.; Kim, S.S. Effects of Na nonstoichiometry in $(Bi_{0.5}Na_{0.5+x})TiO_3$ ceramics. *Appl. Phys. Lett.* **2010**, *96*, 022901:1-022901:3.
85. Xu, Q.; Huang, D.P.; Chen, M.; Chen, W.; Liu, H.X.; Kim, B.H. Effect of bismuth excess on ferroelectric and piezoelectric properties of a $(Na_{0.5}Bi_{0.5})TiO_3$-$BaTiO_3$ composition near the morphotropic phase boundary. *J. Alloys Compounds* **2009**, *471*, 310-316.
86. Wang, X.X.; Tang, X.G.; Chan, H.L. Electromechanical and ferroelectric properties of $(Bi_{1/2}Na_{1/2})TiO_3$-$(Bi_{1/2}K_{1/2})TiO_3$-$BaTiO_3$ lead-free piezoelectric ceramics. *Appl. Phys. Lett.* **2004**, *85*, 91-93.
87. Chu, B.J.; Chen, D.R.; Li, G.R.; Yin, Q.R. Electrical properties of $Na_{1/2}Bi_{1/2}TiO_3$-$BaTiO_3$ ceramics. *J. Eur. Ceram. Soc.* **2002**, *22*, 2115-2121.
88. Xu, Q.; Chen, M.; Chen, W.; Liu, H.X.; Kim, B.H.; Ahn, B.K. Effect of CoO additive on structure and electrical properties of $(Na_{0.5}Bi_{0.5})(0.93)Ba0.07TiO_3$ ceramics prepared by the citrate method. *Acta Mater.* **2008**, *56*, 642-650.
89. Takenaka, T.; Nagata, H.; Hiruma, Y. Phase transition temperatures and piezoelectric properties of $(Bi_{1/2}Na_{1/2})TiO_3$- and $(Bi_{1/2}K_{1/2})TiO_3$-based bismuth perovskite lead-free ferroelectric ceramics. *IEEE T. Ultrason. Ferroelectr.* **2009**, *56*, 1595-1612.
90. Messing, G.L.; Trolier-McKinstry, S.; Sabolsky, E.M.; Duran, C.; Kwon, S.; Brahmaroutu, B.; Park, P.; Yilmaz, H.; Rehrig, P.W.; Eitel, K.B.; Suvaci, E.; Seabaugh, M.; Oh, K.S. Templated grain growth of textured piezoelectric ceramics. *Crit. Rev. Solid State Mat. Sci.* **2004**, *29*, 45-96.
91. Saito, Y.; Takao, H.; Tani, T.; Nonoyama, T.; Takatori, K.; Homma, T.; Nagaya, T.; Nakamura, M. Lead-free piezoceramics. *Nature* **2004**, *432*, 84-87.
92. Yilmaz, H.; Messing G.L.; Trolier-McKinstry, S. (Reactive) templated grain growth of textured sodium bismuth titanate ($Na_{1/2}Bi_{1/2}TiO_3$-$BaTiO_3$) ceramics—I processing. *J. Electroceram.* **2003**, *11*, 207-215.
93. Yan, Y.K.; Zhou, H.P.; Zhao, W.; Liu, D. Fabrication and electrical properties of textured $Na_{1/2}Bi_{1/2}TiO_3$-$BaTiO_3$ ceramics by reactive-templated grain growth. *J. Electroceram.* **2008**, *21*, 246-250.
94. Motohashi, T.; Kimura, T. Development of texture in $Bi_{0.5}Na_{0.5}TiO_3$ prepared by reactive-templated grain growth process. *J. Eur. Ceram. Soc.* **2007**, *27*, 3633-3636.
95. Tani, T.; Kimura, T. Reactive-templated grain growth processing for lead free piezoelectric ceramics. *Adv. Appl. Ceram.* **2006**, *105*, 55-63.

96. Babu, J.B.; Madeswaran, G.; He, M.; Zhang, D.F.; Chen X.L.; Dhanasekaran, R. Inhomogeneity issues in the growth of $Na_{1/2}Bi_{1/2}TiO_3$-$BaTiO_3$ single crystals. *J. Cryst. Growth* **2008**, *310*, 467-472.
97. Sun, R.; Zhang, Q.; Fang, B.; Jiao, J.; Li, X.; Zhao, X.; Lin, D.B.; Wang. D.; Luo, H. Dielectric, electromechanical coupling properties of Mn-doped $Na_{0.5}Bi_{0.5}TiO_3$-$BaTiO_3$ lead-free single crystal. *Appl. Phys. A-Mat. Sci. Process.* **2011**, *103*, 199-205.
98. Chen, Y.; Jiang, X.P.; Luo, H.S.; Dai, J.Y.; Chan, H.L. High-frequency ultrasonic transducer fabricated with lead-free piezoelectric single crystal. *IEEE T. Ultrason. Ferroelectr.* **2010**, *57*, 2601-2604.
99. Zhang, S.T.; Kounga, A.B.; Aulbach, E.; Ehrenberg, H.; Rodel, J. Giant strain in lead-free piezoceramics $Bi_{0.5}Na_{0.5}TiO_3$-$BaTiO_3$-$K_{0.5}Na_{0.5}NbO_3$ system. *Appl. Phys. Lett.* **2007**, *91*, 112906:1-112906:3.
100. Zhang, S.T.; Kounga, A.B.; Aulbach, E.; Granzow, T.; Jo, W.; Kleebe, H.J.; Rodel, J. Lead-free piezoceramics with giant strain in the system $Bi_{0.5}Na_{0.5}TiO_3$-$BaTiO_3$-$K_{0.5}Na_{0.5}NbO_3$. I. Structure and room temperature properties. *J. Appl. Phys.* **2008**, *103*, 034107:1-034107:8.
101. Zhang, S.T.; Kounga, A.B.; Aulbach, E.; Jo, W.; Granzow, T.; Ehrenberg. H.; Rodel, J. Lead-free piezoceramics with giant strain in the system $Bi_{0.5}Na_{0.5}TiO_3$-$BaTiO_3$-$K_{0.5}Na_{0.5}NbO_3$. II. Temperature dependent properties. *J. Appl. Phys.* **2008**, *103*, 034108:1-034108:7.
102. Daniels, J.E.; Jo, W.; Rodel. J.; Jones, J.L. Electric-field-induced phase transformation at a lead-free morphotropic phase boundary: Case study in a 93%$(Bi_{0.5}Na_{0.5})TiO_3$-7% $BaTiO_3$ piezoelectric ceramic. *Appl. Phys. Lett.* **2009**, *95*, 032904:1-032904:3.
103. Jo, W.; Granzow, T.; Aulbach, E.; Rodel, J.; Damjanovic, D. Origin of the large strain response in $(K_{0.5}Na_{0.5})NbO_3$-modified $(Bi_{0.5}Na_{0.5})TiO_3$-$BaTiO_3$ lead-free piezoceramics. *J. Appl. Phys.* **2009**, *105*, 094102:1-094102:5.
104. Tan, X.; Aulbach, E.; Jo, W.; Granzow, T.; Kling, J.; Marsilius, M.; Kleebe, H.J.; Rodel, J. Effect of uniaxial stress on ferroelectric behavior of $(Bi_{1/2}Na_{1/2})TiO_3$-based lead-free piezoelectric ceramics. *J. Appl. Phys.* **2009**, *106*, 044107:1-044107:7.
105. Yang, R.Y.; Lin, M.H.; Lu, H.Y. Core-shell structures in pressureless-sintered undoped $Pb(Fe_{2/3}W_{1/3})O_3$ ceramics. *Acta Mater.* **2001**, *49*, 2597-2607.
106. Egertonand, L.; Bieling, C.A. Isostatically hot-pressed sodium-potassium niobate transducer material for ultrasonic devices. *Amer. Ceram. Soc. Bull.* **1968**, *47*, 1151-1156.
107. Jaeger, R.E.; Egerton, L. Hot pressing of potassium-sodium niobate. *J. Amer. Ceram. Soc.* **1962**, *45*, 209-213.
108. Haertling, G.H. Properties of hot pressed ferroelectric alkali niobate ceramics. *J. Amer. Ceram. Soc.* **1967**, *50*, 329-330.
109. Wu, J.G.; Xiao, D.Q.; Wang, Y.Y.; Zhu, J.G.; Yu, P.; Jiang, Y.H. Compositional dependence of phase structure and electrical properties in $(K_{0.42}Na_{0.58})NbO_3$-$LiSbO_3$ lead-free ceramics. *J Appl. Phys.* **2007**, *102*, 114113:1-114113:5.
110. Li, J.F.; Wang, K.; Zhang, B.P.; Zhang, L.M. Ferroelectric and piezoelectric properties of fine-grained Na0.5K0.5NbO3 lead-free piezoelectric ceramics prepared by spark plasma sintering. *J. Amer. Ceram. Soc.* **2006**, *89*, 706-709.

111. Ahn, C.W.; Park, C.S.; Viehland, D.; Nahm, S.; Kang, D.H.; Bae, K.S.; Priya, S. Correlation between phase transitions and piezoelectric properties in lead-free (K,Na,Li)NbO_3-$BaTiO_3$ ceramics. *Jpn. J. Appl. Phys.* **2008**, *47*, 8880-8883.
112. Tennery, V.J.; Hang, K.W. Thermal and X-ray diffraction studies of the $NaNbO_3$-$KNbO_3$ system. *J. Appl. Phys.* **1968**, *39*, 4749-4753.
113. Wu, L.; Zhang, J.L.; Wang, C.L.; Li, J.C. Influence of compositional ratio K/Na on physical properties in $(K_xNa_{1-x})NbO_3$ ceramics. *J. Appl. Phys.* **2008**, *103*, 084116:1-084116:5.
114. Zhao, P.; Zhang, B.P.; Li, J.F. High piezoelectric d(33) coefficient in Li-modified lead-free (Na,K)NbO_3 ceramics sintered at optimal temperature. *Appl. Phys. Lett.* **2007**, *90*, 242909:1-242909:3.
115. Zhang, Q.; Zhang, B.P.; Li, H.T.; Shang, P.P. Effects of Sb content on electrical properties of lead-free piezoelectric $[(Na_{0.535}K_{0.480})_{0.942}Li_{0.058}](Nb_{1-x}Sb_x)O_3$ ceramics. *J. Alloys Compounds* **2010**, *490*, 260-263.
116. Kusumoto, K. Dielectric And piezoelectric properties Of Nanbo3-Batio3-Srtio3 Ceramics. In *Proceedings of the Applications of Ferroelectrics, ISAF 2007, Sixteenth IEEE International Symposium*, Nara, Japan, 27–31 May 2007; pp. 686-687, doi:10.1109/ISAF.2007.4393370.
117. Maurya, D.; Ahn, C.W.; Zhang, S.; Priya, S. High dielectric composition in the system Sn-modified $(1-x)BaTiO_3$-$xBa(Cu_{1/3}Nb_{2/3})O_3$, x = 0.025 for multilayer ceramic capacitor. *J. Amer. Ceram. Soc.* **2010**, *93*, 1225-1228.
118. Yuan, Y.; Zhang, S.R.; Zhou, X.H.; Liu, J.S. Phase transition and temperature dependences of electrical properties of $[Bi_{0.5}(Na_{1-x-y}K_xLi_y)_{0.5}]TiO_3$ ceramics. *Jpn. J. Appl. Phys.* **2006**, *45*, 831-834.
119. Takenaka, T.; Nagata, H. Current status and prospects of lead-free piezoelectric ceramics. *J. Eur. Ceram. Soc.* **2005**, *25*, 2693-2700.
120. Chen, M.; Xu, Q.; Kim, B.H.; Ahn, B.K.; Ko, J.H.; Kang, W.J.; Nam, O.J. Structure and electrical properties of $(Na_{0.5}Bi_{0.5})_{(1-x)}Ba_xTiO_3$ piezoelectric ceramics. *J. Eur. Ceram. Soc.* **2008**, *28*, 843-849.
121. Xu, C.G.; Lin, D.M.; Kwok, K.W. Structure, electrical properties and depolarization temperature of $(Bi_{0.5}Na_{0.5})TiO_3$-$BaTiO_3$ lead-free piezoelectric ceramics. *Solid State Sci.* **2008**, *10*, 934-940.
122. Zhou, D.X.; Li, H.; Gong, S.P.; Hu, Y.X.; Han, K. Sodium bismuth titanate-based lead-free piezoceramics prepared by aqueous gelcasting. *J. Amer. Ceram. Soc.* **2008**, *91*, 2792-2796.
122. Oh, T.; Kim, M. Phase relation and dielectric properties in $(Bi_{1/2}Na_{1/2})_{(1-x)}Ba_xTiO_3$ lead-free ceramics. *Mater. Sci. Eng. B Solid State M.* **2006**, *132*, 239-246.
124. Gomah-Pettry, J.R.; Said, E.; Marchet, P.; Mercurio, J.P. Sodium-bismuth titanate based lead-free ferroelectric materials. *J. Eur. Ceram. Soc.* **2004**, *24*, 1165-1169.
125. Lin, D.B.; Kwok, K.W.; Chan, H.L. Structure and electrical properties of $Bi_{0.5}Na_{0.5}TiO_3$-$BaTiO_3$-$Bi_{0.5}Li_{0.5}TiO_3$ lead-free piezoelectric ceramics. *Solid State Ionics* **2008**, *178*, 1930-1937.
126. Lin, D.M.; Xiao, D.Q.; Zhu, J.G.; Yu, P. Piezoelectric and ferroelectric properties of lead-free $[Bi_{1-y}(Na_{1-x-y}Li_x)]_{0.5}Ba_yTiO_3$ ceramics. *J. Eur. Ceram. Soc.* **2006**, *26*, 3247-3251.
127. Yang, Z.; Liu, B.; Wei, L.; Hou, Y. Structure and electrical properties of $(1-x)Bi_{0.5}Na_{0.5}TiO_3-xBi_{0.5}K_{0.5}TiO_3$ ceramics near morphotropic phase boundary. *Mater. Res. Bull.* **2008**, *43*, 81-89.

128. Yoshii, K.; Hiruma, Y.; Nagata, H.; Takenaka, T. Electrical properties and depolarization temperature of $(Bi_{1/2}Na_{1/2})TiO_3$-$(Bi_{1/2}K_{1/2})TiO_3$ lead-free piezoelectric ceramics. *Jpn. J. Appl. Phys. Pt 1* **2006**, *45*, 4493-4496.
129. Zhao, S.C.; Li, G.R.; Ding, A.L.; Wang, T.B.; Yin, Q.R. Ferroelectric and piezoelectric properties of $(Na, K)_{0.5}Bi_{0.5}TiO_3$ lead free ceramics. *J. Phys.-D-Appl. Phys.* **2006**, *39*, 2277-2281.
130. Zhang, Y.R.; Li, J.F.; Zhang, B.P. Enhancing electrical properties in NBT-KBT lead-free piezoelectric ceramics by optimizing sintering temperature. *J. Amer. Ceram. Soc.* **2008**, *91*, 2716-2719.
131. Hiruma, Y.; Yoshii, K.; Nagata, H.; Takenaka, T. Phase transition temperature and electrical properties of $(Bi_{1/2}Na_{1/2})TiO_3$-$(Bi_{(1/2)}A_{(1/2)})TiO_3$ (A=Li and K) lead-free ferroelectric ceramics. *J. Appl. Phys.* **2008**, *103*, 084121:1-084121:7.
132. Oh, T. Dielectric relaxor properties in the system of $(Na_{1-x}K_x)_{(1/2)}Bi_{1/2}TiO_3$ ceramics. *Jpn. J. Appl. Phys. Pt. 1* **2006**, *45*, 5138-5143.
133. Egerton L.; Dillon, D.M. Piezoelectric and Dielectric properties of ceramics in the system of Potassium sodium niobate. *J. Amer. Ceram. Soc.* **1959**, *42*, 438-442.
134. Hollenstein, E.; Davis, M.; Damjanovic, D.; Setter, N. Piezoelectric properties of Li- and Ta-modified $(K_{0.5}Na_{0.5})NbO_3$ ceramics. *Appl. Phys. Lett.* **2005**, *87*, 182905:1-182905:3.
135. Lang, S.B.; Zhu, W.Y.; Cross, L.E. Piezoelectric and pyroelectric properties of $(K_{0.5}Na_{0.5})_{(1-x)}(Nb_{1-y}Ta_y)O_3$ ceramics. *Ferroelectrics* **2006**, *336*, 15-21.
136. Ahn, C.W.; Maurya, D.; Park, C.S.; Nahm, S.; Priya, S. A generalized rule for large piezoelectric response in perovskite oxide ceramics and its application for design of lead-free compositions. *J. Appl. Phys.* **2009**, *105*, 114108:1-114108:6.
137. Lin, D.B.; Li, Z.R.; Zhang, S.; Xu, Z.; Yao, X. Dielectric/piezoelectric properties and temperature dependence of domain structure evolution in lead free $(K_{0.5}Na_{0.5})NbO_3$ single crystal. *Solid State Commun.* **2009**, *149*, 1646-1649.
138. Lin, D.B.; Li, Z.R.; Zhang, S.; Xu, Z.; Yao, X. Influence of MnO_2 doping on the dielectric and piezoelectric properties and the domain structure in $(K_{0.5}Na_{0.5})NbO_3$ single crystals. *J. Amer. Ceram. Soc.* **2010**, *93*, 941-944.
139. Xu, G.S.; Yang, D.F.; Chen, K.; Payne, D.A.; Carroll, J.F. Growth, domain dynamics and piezoelectric properties of some lead-free ferroelectric crystals. *J. Electroceram.* **2010**, *24*, 226-230.
140. Chang, Y.F.; Poterala, S.F.; Yang, Z.P.; Trolier-McKinstry, S.; Messing, G.L. <001> textured $(K_{0.5}Na_{0.5})(Nb_{0.97}Sb_{0.03})O_3$ piezoelectric ceramics with high electromechanical coupling over a broad temperature range. *Appl. Phys. Lett.* **2009**, *95*, 232905:1-232905:3.
141. Pertsev, N.A.; Zembilgotov, A.G.; Tagantsev, A.K. Effect of mechanical boundary conditions on phase diagrams of epitaxial ferroelectric thin films. *Phys. Rev. Lett.* **1998**, *80*, 1988-1991.
142. Morelli, A.; Venkatesan, S.; Kooi, B.J.; Palasantzas, G.; De Hosson, J.T. Piezoelectric properties of $PbTiO_3$ thin films characterized with piezoresponse force and high resolution transmission electron microscopy. *J. Appl. Phys.* **2009**, *105*, 064106:1-064106:6.
143. Petraru, A.; Pertsev, N.A.; Kohlstedt, H.; Poppe, U.; Waser, R.; Solbach, A.; Klemradt, U. Polarization and lattice strains in epitaxial BaTiO3 films grown by high-pressure sputtering. *J. Appl. Phys.* **2007**, *101*, 114106:1-114106:8.

144. Li, Y.L.; Cross, L.E.; Chen, L.Q. A phenomenological thermodynamic potential for $BaTiO_3$ single crystals. *J. Appl. Phys.* **2005**, *98*, 064101:1-064101:4.
145. Liang, L.Y.; Li, Y.L.; Chen, L.Q.; Hu, S.Y.; Lu, G.H. Thermodynamics and ferroelectric properties of $KNbO_3$. *J. Appl. Phys.* **2009**, *106*, 104118:1-104118:9.
146. Matsubara, M.; Yamaguchi, T.; Sakamoto, W.; Kikuta, K.; Yogo, T.; Hirano, S. Processing and piezoelectric properties of lead-free (K,Na)(Nb,Ta)O_3 ceramics. *J. Amer. Ceram. Soc.* **2005**, *88*, 1190-1196.
147. Matsubara, M.; Yamaguchi, T.; Kikuta, K.; Hirano, S. Sinterability and piezoelectric properties of (K,Na)NbO_3 ceramics with novel sintering aid. *Jpn. J. Appl. Phys. Pt. 1* **2004**, *43*, 7159-7163.
148. Lim, J.B.; Zhang, S.; Jeon J.H.; Shrout, T.R. (K,Na)NbO_3-based ceramics for piezoelectric hard lead-free materials. *J. Amer. Ceram. Soc.* **2010**, *93*, 1218-1220.
149. Zakharov, A.Yu.; Bichurin, M.I. *Generalized Lattice Model of Multi-Component Systems with Internal Degrees of Freedom—I General Consideration*. 9 September 2008; p. 17, arXiv:0809.1495v1 [cond-mat.stat-mech].
150. Zakharov, A.Yu.; Bichurin, M.I. Lattice models in condensed matter theory. *Nanostruct. Math. Phys. Model.* **2010**, *2*, 25-53, (In Russian).
151. Zakharov, A.Yu.; Bichurin, M.I. Generalized lattice model of multi-component systems with internal degrees of freedom—II Quasiequilibrium States. Cornell University Library, Ithaca, NY, USA, 5 October 2009; p. 12, arXiv:0910.0861v1 [cond-mat.stat-mech].
152. Zakharov, A.Yu.; Bichurin, M.I.; Priya, S. *On the Theory of Ferroelectric Solid Solutions*. Cornell University Library, Ithaca, NY, USA, 2 December 2010; p. 7, arXiv:1012.0594v1 [cond-mat.mtrl-sci].
153. Debye, P. *Polar Molecules*, 1st ed.; Lancaster Press Inc: Lancaster, PA, USA, 1929; pp. 1-172.
154. Brown, W.F., Jr. Dielectrics. In *Handbuch der Physik*, 1st ed.; Flügge, S., Ed.; Springer-Verlag: Berlin, Germany, 1956; Volume XVII, Chapter 1, pp. 1-326.
155. Fröhlich, H. *Theory of Dielectrics: Dielectric Constant and Dielectric Loss*, 1st ed.; Clarendon Press: London, UK, 1958; pp. 1-180.
156. Shirane G.; Suzuki, K. On the phase transition in barium-lead titanate. *J. Phys. Soc. Jpn.* **1951**, *6*, 274-278.
157. Landolt, H., Börnstein, R. *Numerical Data and Functional Relationships in Science and Technology—New Series, Group III, Condensed Matter, Electrical Properties, Ferroelectrics and Related Substances, Oxides*, 1st ed.; Springer-Verlag: Berlin, Germany, 2002; Volume 36A1, pp. 1-588.
158. Petrov, V.M.; Bichurin, M.I.; Laletin, V.M.; Paddubnaya, N.; Srinivasan, G. Modeling of magnetoelectric effects in ferromagnetic/piezoelectric bulk composites. In *Proceedings of the 5th International Conference on Magnetoelectric Interaction Phenomena in Crystals, MEIPIC-5*, Sudak, Ukraine, 21–24 September 2003; arXiv:cond-mat/0401645.
159. Harshe, G.; Dougherty, J.P.; Newnham, R.E. Theoretical modelling of 3-0/0-3 magnetoelectric composites. *Int. J. Appl. Electromagn. Mat.* **1993**, *4*, 161-171.
160. Landolt, H.; Börnstein, R. *Numerical Data and Functional Relationships in Science and Technology—New Series, Group III, Crystal and Solid State Physics*, 1st ed.; Springer-Verlag: Berlin, Germany, 1970; Volume 4B, pp. 1-779.

161. Ahn, C.W.; Maurya, D.; Park, C.S.; Nahm, S.; Priya, S. A generalized rule for large piezoelectric response in perovskite oxide ceramics and its application for design of lead-free compositions. *J. Appl. Phys.* **2009**, *105*, 114108:1-114108:6.
162. Ahn, C.W.; Choi, C.H.; Park, H.Y.; Nahm, S.; Priya, S. Dielectric and piezoelectric properties of $(1-x)(Na_{0.5}K_{0.5})NbO_3-xBaTiO_3$ ceramics. *J. Mater. Sci.* **2008**, *43*, 6784-6797.
163. Echigoya, J.; Hayashi, S.; Obi, Y. Directional solidification and interface structure of BaTiO3-CoFe2O4 eutectic. *J. Mater. Sci.* **2000**, *35*, 5587-5591.
164. Islam, R.A.; Priya, S. Large magnetoelectric coefficient in Co-fired Pb $(Zr_{0.52}Ti_{0.48})O_3$-$Pb(Zn_{1/3}Nb_{2/3})O_3$-$Ni_{0.6}Cu_{0.2}Zn_{0.2}Fe_2O_4$ trilayer magnetoelectric composites. *J. Mater. Sci.* **2008**, *43*, 2072-2076.
165. Islam, R.A.; Ni, Y.; Khachaturyan, A.G.; Priya, S. Giant magnetoelectric effect in sintered multilayered composite structures. *J. Appl. Phys.* **2008**, *104*, 044103:1-044103:5.
166. Islam, R.A.; Rong, C.B.; Liu, J.P.; Priya, S. Effect of gradient composite structure in cofired bilayer composites of $Pb(Zr_{0.56}Ti_{0.44})O_3$-$Ni_{0.6}Zn_{0.2}Cu_{0.2}Fe_2O_4$ system on magnetoelectric coefficient. *J. Mater. Sci.* **2008**, *43*, 6337-6343.
167. Islam, R.A.; Priya, S. Effect of piezoelectric grain size on magnetoelectric coefficient of $Pb(Zr_{0.52}Ti_{0.48})O_3$-$Ni_{0.8}Zn_{0.2}Fe_2O_4$ particulate composites. *J. Mater. Sci.* **2008**, *43*, 3560-3568.
168. Grossinger, R.; Duong, G.V.; Sato-Turtelli, R. The physics of magnetoelectric composites. *J. Magn. Magn. Mater.* **2008**, *320*, 1972-1977.
169. Bedekar, V.; Poudyal, N.; Rong, C.B.; Liu, J.P.; Kim, C.U.; Priya, S. Improved magnetoelectric properties of piezoelectric-magnetostrictive nanocomposites synthesized using high-pressure compaction technique. *J. Mater. Sci.* **2009**, *44*, 2162-2166.
170. Yang, S.C.; Park C.S.; Cho, K.H.; Priya, S. Self-biased magnetoelectric response in three-phase laminates. *J. Appl. Phys.* **2010**, *108*, 093706:1-093706:6.
171. Priya, S.; Islam, R.A.; Dong, S.X.; Viehland, D. Recent advancements in magnetoelectric particulate and laminate composites. *J. Electroceram.* **2007**, *19*, 147-164.
172. Zhai, J.Y.; Xing, Z.P.; Dong, S.X.; Li, J.F.; Viehland, D. Magnetoelectric laminate composites: An overview. *J. Amer. Ceram. Soc.* **2008**, *91*, 351-358.
173. Islam, R.A.; Priya, S. Magnetoelectric properties of the lead-free cofired $BaTiO_3$-$(Ni_{0.8}Zn_{0.2})Fe_2O_4$ bilayer composite. *Appl. Phys. Lett.* **2006**, *89*, 152911:1-152911:3.
174. Nan, C.W.; Li, M.; Huang, J.H. Calculations of giant magnetoelectric effects in ferroic composites of rare-earth-iron alloys and ferroelectric polymers. *Phys. Rev. B* **2001**, *63*, 144415:1-144415:9.
175. Ruy, J.; Priya, S.; Carazo, A.V.; Uchino, K.; Kim, H.E. Effect of the magnetostrictive layer on magnetoelectric properties in lead zirconate titanate/terfenol-d laminate composites. *J. Amer. Ceram. Soc.* **2001**, *84*, 2905-2908.
176. Park, C.S.; Cho, K.H.; Arat, M.A.; Evey, J.; Priya, S. High magnetic field sensitivity in $Pb(Zr,Ti)O_3$–$Pb(Mg_{1/3}Nb_{2/3})O_3$ single crystal/Terfenol-D/Metglas magnetoelectric laminate composites. *J. Appl. Phys.* **2010**, *107*, 094109:1-094109:4.
177. Islam, R.A.; Priya, S. ME response of cofired trilayer magnetoelectric composites with partial texturing. *J. Mater. Sci.* **2009**, *44*, 5935-5938.

178. Park, C.S.; Ahn, C.W.; Ryu, J.; Yoon, W.H.; Park, D.S.; Kim, H.E.; Priya, S. Design and characterization of broadband magnetoelectric sensor. *J. Appl. Phys.* **2009**, *105*, 094111:1-094111:6.
179. Park, C.S.; Ahn, C.W.; Yang, S.C.; Priya, S. Dimensionally gradient magnetoelectric bimorph structure exhibiting wide frequency and magnetic dc bias operating range. *J. Appl. Phys.* **2009**, *106*, 114101:1-114101:5.
180. Cho, K.H.; Park, C.S.; Priya, S. Effect of intensive and extensive loss factors on the dynamic response of magnetoelectric laminates. *Appl. Phys. Lett.* **2010**, *97*, 182902:1-182902:3.
181. Yang, S.C.; Park, C.S.; Cho, K.H.; Priya, S. Self-biased magnetoelectric response in three-phase laminates. *J. Appl. Phys.* **2010**, *108*, 093706:1-09706:6.
182. Gebhardt, S.; Schonecker, A.; Steinhausen, R.; Seifert, W.; Beige, H. Quasistatic and dynamic properties of 1-3 composites made by soft molding. *J. Eur. Ceram. Soc.* **2003**, *23*, 153-159.
183. Lam, K.H.; Lo, C.Y.; Chan, H.L. Frequency response of magnetoelectric 1-3-type composites. *J. Appl. Phys.* **2010**, *107*, 093901:1-093901:5.
184. Shi, Z.; Nan, C.W.; Zhang, J.; Ma, J.; Li, J.F. Magnetoelectric properties of multiferroic composites with pseudo-1-3-type structure. *J. Appl. Phys.* **2006**, *99*, 124108:1-124108:5.
185. Petrov, V.M.; Srinivasan, G.; Bichurin, M.I.; Gupta, A. Theory of magnetoelectric effects in ferrite piezoelectric nanocomposites. *Phys. Rev. B* **2007**, *75*, 224407:1-224407:6.
186. Park, C.S.; Ahn, C.; Priya, S. Enhanced magnetoelectric properties in three-phase composites with 2-1-2 connectivity. *Phil. Mag.* **2010**, *90*, 4443-4452.